SYNTHESIS AND APPLICATIONS OF ION INCORPORATED AMORPHOUS CALCIUM-MAGNESIUM CARBONATE

A THESIS SUBMITTED TO
THE GRADUATE SCHOOL OF NATURAL AND APPLIED SCIENCES
OF
MIDDLE EAST TECHNICAL UNIVERSITY

BY

YAĞMUR GÖÇTÜ

IN PARTIAL FULFILLMENT OF THE REQUIREMENTS
FOR
THE DEGREE OF MASTER OF SCIENCE
IN
METALLURGICAL AND MATERIALS ENGINEERING

JANUARY 2023

Approval of the thesis:

SYNTHESIS AND APPLICATIONS OF ION INCORPORATED AMORPHOUS CALCIUM-MAGNESIUM CARBONATE

submitted by **YAĞMUR GÖÇTÜ** in partial fulfillment of the requirements for the degree of **Master of Science** i**n Metallurgical and Materials Engineering, Middle East Technical University** by,

Prof. Dr. Halil Kalıpçılar
Dean, Graduate School of **Natural and Applied Sciences** _____

Prof. Dr. Ali Kalkanlı
Head of the Department, **Metallurgical and Materials Eng.** _____

Assoc. Prof. Dr. Batur Ercan
Supervisor, **Metallurgical and Materials Engineering, METU** _____

Examining Committee Members:

Prof. Dr. Abdullah Öztürk
Metallurgical and Materials Engineering, METU _____

Assoc. Prof. Dr. Batur Ercan
Metallurgical and Materials Engineering,METU _____

Prof. Dr. Cevdet Kaynak
Metallurgical and Materials Engineering, METU _____

Assist. Prof. Dr. Yusuf Keleştemur
Metallurgical and Materials Engineering, METU _____

Assoc. Prof. Dr. Sedat Odabaş
Chemistry, Ankara University _____

Date: 18.01.2023

I hereby declare that all information in this document has been obtained and presented in accordance with academic rules and ethical conduct. I also declare that, as required by these rules and conduct, I have fully cited and referenced all material and results that are not original to this work.

Name Last name : Yağmur Göçtü

Signature :

ABSTRACT

SYNTHESIS AND APPLICATIONS OF ION INCORPORATED AMORPHOUS CALCIUM-MAGNESIUM CARBONATE

Göçtü, Yağmur
Master of Science, Metallurgical and Materials Engineering
Supervisor : Assoc. Prof. Dr. Batur Ercan

January 2023, 55 pages

Amorphous calcium carbonate (ACC) can be synthesized using co-precipitation technique and different ions can typically be incorporated into its amorphous structure to enhance its stability. Although ACC was investigated for various applications, its antibacterial properties have not been explored. In this thesis, two different types of magnesium stabilized amorphous calcium carbonate (ACMC) nanoparticles were synthesized for antibacterial applications. In the first part selenite ions, and in the second part zinc and strontium ions were incorporated into the ACMC nanoparticles. It was shown that ion incorporated ACMC nanoparticles maintained their amorphous structure. The synthesized nanoparticles inhibited bacterial growth of several bacteria strains. 0.01, 0.005 and 0.001 M selenite incorporated ACMC nanoparticles prepared at 1 g/L concentration significantly inhibited the growth of gram-positive *Staphylococcus aureus* (*S. aureus*) and *Staphylococcus epidermidis* (*S. epidermidis*) and gram-negative *Escherichia coli* (*E. coli*) and *Pseudomonas aeruginosa* (*P. aeruginosa*) strains after 24 h of interaction. The antibacterial activity was shown to enhance as the amount of incorporated selenite was increased. On the other hand, zinc and/or strontium incorporated (0.1

and 0.01 M) ACMC nanoparticles prepared at 0.01 g/L concentration exerted antibacterial activity towards *S. aureus*, and the extend of this antibacterial activity could also be enhanced by ion concentration, where higher amounts (0.1 M) of Zn and Sr incorporated ACMC nanoparticles were able to decrease the growth of *E. coli*. In summary, in this thesis study, non-toxic and biodegradable nanoparticles were fabricated by incorporating selenite, zinc and strontium into ACMC for antibacterial applications. Results showed that ion incorporated ACMC is a potential candidate to fight with bacteria.

Keywords: Calcium carbonate, amorphous, stabilization, ion incorporation, antibacterial

ÖZ

İYON KATKILI AMORF KALSİYUM-MAGNEZYUM KARBONAT SENTEZİ VE KULLANIM ALANLARI

Göçtü, Yağmur

Yüksek Lisans, Metalurji ve Malzeme Mühendisliği
Tez Yöneticisi: Doç. Dr. Batur Ercan

Ocak 2023, 55 sayfa

Amorf kalsiyum karbonat (ACC) birlikte çökeltme tekniği kullanılarak sentezlenebilir ve stabilitesini arttırmak için tipik olarak amorf yapısına farklı iyonlar dahil edilebilir. ACC çeşitli uygulamalar için araştırılmış olmasına rağmen, antibakteriyel özellikleri araştırılmamıştır. Bu tezde, antibakteriyel uygulamalar için iki farklı tipte magnezyumla stabilize edilmiş amorf kalsiyum karbonat (ACMC) nanoparçacıkları sentezlenmiştir. Birincisinde selenit, ikincisinde çinko ve stronsiyum iyonları ACMC nanoparçacıklarına katkılanmış ve nanoparçacıkların amorf yapılarını koruduğu görülmüştür. Sentezlenen nanoparçacıkların çeşitli bakteri suşlarına karşı bakteri çoğalmasını azaltıcı etki gösterdiği gösterilmiştir. 1 g/L konsantrasyonda hazırlanan 0,01, 0,005 ve 0,001 M selenit katkılı ACMC nanoparçacıkları 24 saatlik etkileşim sonucunda hem gram pozitif *Staphylococcus aureus* (*S. aureus*) ve *Staphylococcus epidermidis* (*S. epidermidis*) hem de gram negatif *Escherichia coli* (*E. coli*) ve *Pseudomonas aeruginosa* (*P. aeruginosa*) bakterileri suşlarının bakteriyel büyümesini önemli ölçüde inhibe etmiştir. ACMC'ye katkılanan selenit miktarı arttıkça antibakteriyel etkinin de arttığı gösterilmiştir. Öte yandan, 0,01 g/L konsantrasyonda hazırlanan 0,1 ve 0,01 M çinko ve/veya

stronsiyum katkılı ACMC nanoparçacıkları, *S. aureus*'un bakteriyel çoğalmasını azaltmıştır ve bu antibakteriyel etkinin kapsamı, katkılanan Zn ve Sr iyon miktarı arttırılarak geliştirilmiştir. Öyle ki yalnızca Zn ve Sr'nin birlikte ve yüksek miktarda (0,1 M) katkılandığı ACMC nanoparçacıkları, *E. coli*'nin büyümesini kısmen azaltabilmiştir. Özetle, bu tez çalışmasında ACMC'ye selenit, çinko ve stronsiyum ekleyerek antibakteriyel uygulamalar için toksik olmayan, biyobozunur ve antibakteriyel nanoparçacıklar sunulmuştur. Sonuçlar, iyon katkılı ACMC'nin bakterilerle savaşmak için potansiyel bir aday olduğunu göstermiştir.

Anahtar Kelimeler: Kalsiyum karbonat, amorf, stabilizasyon, iyon katkısı, antibakteriyel

To my family

and

To the victims of Turkey-Syria Earthquake

ACKNOWLEDGMENTS

First and foremost, I would like to express my deepest gratitude to my supervisor Assoc. Prof. Dr. Batur Ercan for his mentorship, assistance, advice, insightful comments and criticism, and belief in me at every stage of the research project.

I am deeply thankful to Prof. Dr. Şefik Süzer for sharing his wide knowledge of XPS and valuable comments.

I would like to acknowledge the Middle East Technical University Research Funds (TEZ-YL-308-2022-10852) and The Scientific and Technological Research Council of Turkey (118M652) for providing financial support.

I would like to thank technical assistances of our department; Nilüfer Özel and Serkan Yılmaz for their help in XRD and SEM characterization. My sincere thanks also go to Melisa Kafalı for SEM images and Çağatay Mert Oral for SEM images and XPS characterization, and Yiğithan Tufan for FTIR measurements.

I am genuinely grateful to my dear friends Alper Haliloğlu, Cansu Taşar and Melisa Kafalı for their continuous support, help and beautiful friendship along the way. Also, I express special thanks to Dr. Azade Yelten for her sincere friendship and advice.

Lastly, I want to thank my family, to whom I dedicate my thesis, for their eternal love, support, sacrifices and patience.

TABLE OF CONTENTS

LIST OF TABLES

TABLES

LIST OF FIGURES

FIGURES

LIST OF ABBREVIATIONS

ABBREVIATIONS

ACC: Amorphous calcium carbonate

ACMC: Amorphous calcium-magnesium carbonate

DMEM: Dulbecco's Modified Eagle Medium

FTIR: Fourier transform infrared spectroscopy

MTT: 3- (4,5-dimethyl-2-thiazolyl)-2,5-diphenyl-2H-tetrazolium bromide

SAED: Selected area diffraction

SEM: Scanning electron microscopy

PBS: Phosphate buffer saline

TEM: Transmission electron microscopy

TGA: Thermal gravimetric analysis

TSB: Tryptic soy broth

XRD: X-ray diffraction

E. coli: Escherichia coli

P. aeruginosa: Pseudomonas aeruginosa

S. aureus: Staphylococcus aureus

S. epidermidis: Staphylococcus epidermidis

LIST OF SYMBOLS

SYMBOLS

°: degree

μ: micro

~: approximately

CHAPTER 1

INTRODUCTION

Calcium carbonate ($CaCO_3$) is a well-known mineral used in numerous industries, including paper, painting, coating, filler, adhesive and pharmaceutical [1], [2]. $CaCO_3$ has three anhydrous crystalline polymorphs as vaterite, aragonite and calcite [3]; and two hydrous forms as monohydrocalcite and ikaite [4], [5].

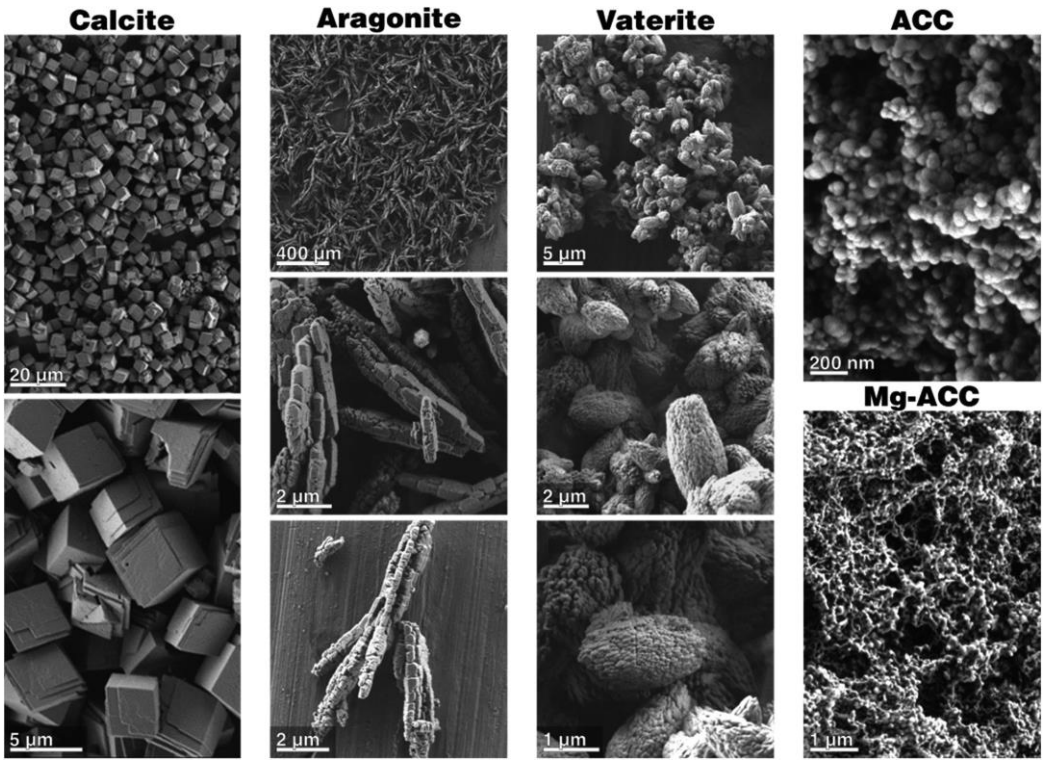

Figure 1.1 Scanning electron microscopy (SEM) images of anhydrous polymorphs of calcium carbonate: calcite, aragonite, vaterite, as well as and amorphous calcium carbonate (ACC) and magnesium stabilized ACC (Mg-ACC) [6]

Aside from its crystalline polymorphs, calcium carbonate can exist in amorphous form as amorphous calcium carbonate (ACC). ACC is the transient precursor of its crystalline counterparts [7] and it has extensive water content in its structure, which plays a key role in its stabilization and transformation [8]. In aqueous environment, due to its highly metastable nature, ACC swiftly transforms to more stable crystalline forms through dissolution and recrystallization [9], [10].

Crystalline polymorphs of $CaCO_3$ can be synthesized using various chemical methods to obtain different polymorphs and morphologies [11], [12]. For instance, Diaz et al. created peanut-like and spherulitic calcite, which was typically found in rhombohedral morphology, in around 300-400 μm size via doping with divalent ions as Mn^{2+} and Co^{2+} in an acidified silica gel environment [13]. Yu et al. synthesized 5 - 6 μm sized flower-like mesoporous calcite using a microwave system followed by a calcination process at 500 °C [14]. Samanta et al. obtained triclinic aragonite with microdumbbell shape consisting of nanorods having 1.5 μm length and 50 nm width using hydrothermal synthesis method at 140 °C [15]. Febrida et al. acquired spherical porous vaterite particles around 177 nm in size by precipitation reaction [16]. Dou et al., utilizing flash nano precipitation method, synthesized vaterite particles having a convex-disc shape with an average particle size of at least 800 nm [17]. Hence, the synthesis of those crystalline polymorphs frequently requires high temperatures and more complex systems, which eventually gives sub-micron sized particles.

On the other hand, among different polymorphs of $CaCO_3$, ACC brings distinct advantages over its crystalline counterparts. Specifically, it can be synthesized to have nanometer sized particles via simple wet chemistry and vapor diffusion techniques, which is challenging for the anhydrous polymorphs [18]. Furthermore, it has a highly pH responsive degradation characteristic, demanded by several

application fields such as medical drug delivery, water treatment and design of novel optical nano-composites [19]. Last but not least, various ions can easily be incorporated to ACC, whereas it might not be possible for some crystalline polymorphs. For instance, phosphate is incompatible with calcite lattice; therefore, the crystallization product consists of a mixture of calcite and hydroxyapatite [20].

1.1 Research Objectives

This research was divided into two parts. In Chapter 4, selenite incorporated ACMC nanoparticles were discussed. Antibacterial paints for houses and hospitals, paper-based hygiene products including paper towel and toilet paper, waste water treatment and coatings to limit microbiologically-induced corrosion are among the applications which use calcium carbonate and, at the same time, require enhanced resistance to bacterial activity. Hence, in Chapter 4, in an attempt to utilize the non-toxic and degradable nature of Mg^{2+} stabilized ACC (ACMC), it was aimed to incorporate antibacterial SeO_3^{2-} ions, and to provide antibacterial characteristics to ACMC. In fact, this is the first study in literature in which selenite incorporated ACMC nanoparticles were synthesized and their antibacterial properties against several bacteria strains were investigated.

In Chapter 5, zinc and strontium incorporated ACMC nanoparticles were analyzed. Having biodegradable and biocompatible nature, along with its biomimetic chemistry consisting of calcium and carbonate ions present in calcified tissues, makes ACC a favorable candidate for biomedical applications. Therefore, in Chapter 5, zinc and strontium ion incorporated magnesium stabilized ACC (ACMC) nanoparticles were aimed to be synthesized for biomedical applications. This is the first study incorporating these ions into ACMC to provide antibacterial activity, while maintaining mammalian cell viability.

The research objectives of this thesis are:

- To synthesize magnesium stabilized amorphous calcium carbonate (ACMC),
- To incorporate selenite, zinc and strontium ions into the ACMC nanoparticles while maintaining nanometer size and amorphous structure,
- To investigate the antibacterial activity of the nanoparticles against several bacteria strains.

CHAPTER 2

LITERATURE REVIEW

In nature, several organisms, such as sea urchins and mollusks, embody both the crystalline and amorphous $CaCO_3$ alongside organic molecules in their hierarchical structure. In fact, it was observed that biogenic ACC derived from living organisms could preserve its stability *in vitro* [21], [22]. Hence, inspired by nature, stabilization of ACC using some acidic macromolecules and ions was investigated [23], [24], [25].

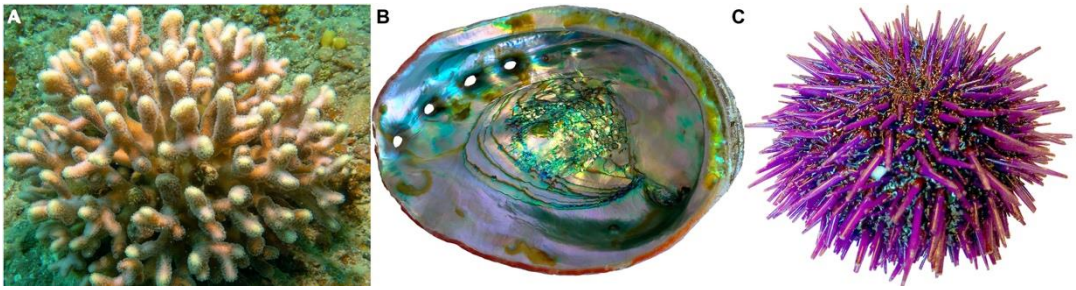

Figure 2.1 Photographs of calcifying organisms: a) coral, b) mollusk and c) sea urchin [26]

In literature, there were various studies in which Mg^{2+} ions were successfully used to stabilize ACC to obtain amorphous calcium-magnesium carbonate (ACMC). It was known that ACC had two forms: hydrous ACC and anhydrous ACC. Hydrous ACC transforms to anhydrous ACC through dehydration, and then, following an energetically downhill path, crystallizes to calcite rapidly [27]. Though the stabilization mechanism of Mg^{2+} on ACC was not clear, it was attributed to creation of a high dehydration free energy barrier, which decelerated calcite nucleation [28].

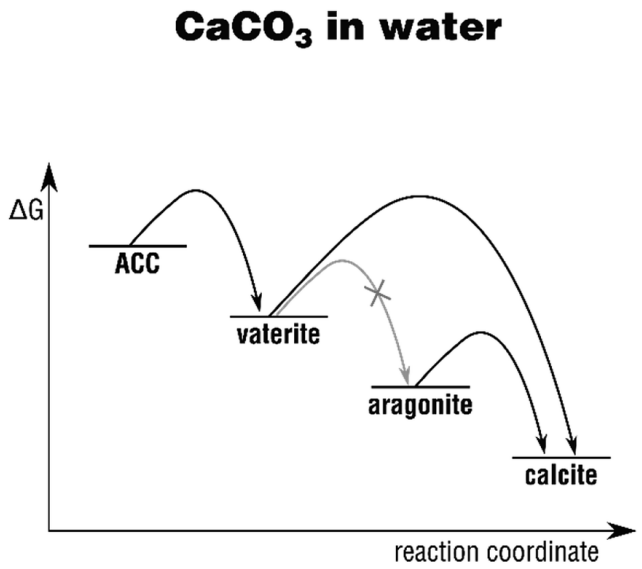

Figure 2.2 Phase transformation and associated Gibbs Free Energy change od calcium carbonate in aqueous medium [6]

ACC is a non-toxic, biodegradable and biocompatible nanomaterial, and therefore, it is a potential candidate for numerous engineering applications. For instance, Xue *et al.* analyzed polymer modified ACC nanoparticles as a drug carrier, and targeted these nanoparticles to tumor cells to utilize their pH dependent degradation and high drug loading capacity [29]. Nie *et al.* investigated sodium alginate and phosphate stabilized ACC nanocarriers and loaded them with curcumin to fight with cancer [25]. Dong *et al.* synthesized gadolinium doped poly (acrylic acid) stabilized ACC as a magnetic resonance (MR) imaging contrast agent due to the extensive water content of ACC [30]. Xu *et al.* proposed ACMC to eliminate phosphate from wastewater due to its high adsorption capacity [31]. Likewise, Jia *et al.* fabricated polymer stabilized ACC for wastewater treatment and showed that the nano-sized particles were quite efficient in exchanging heavy metal ions [32]. ACC was also suggested as a cement additive for self-healing of micro-cracks [33], and upon stabilizing with magnesium it could be used as an ink in 3D printing [34]. In spite of

the potential use of ACC in numerous industrial applications, its efficacy as an antibacterial agent have not been explored.

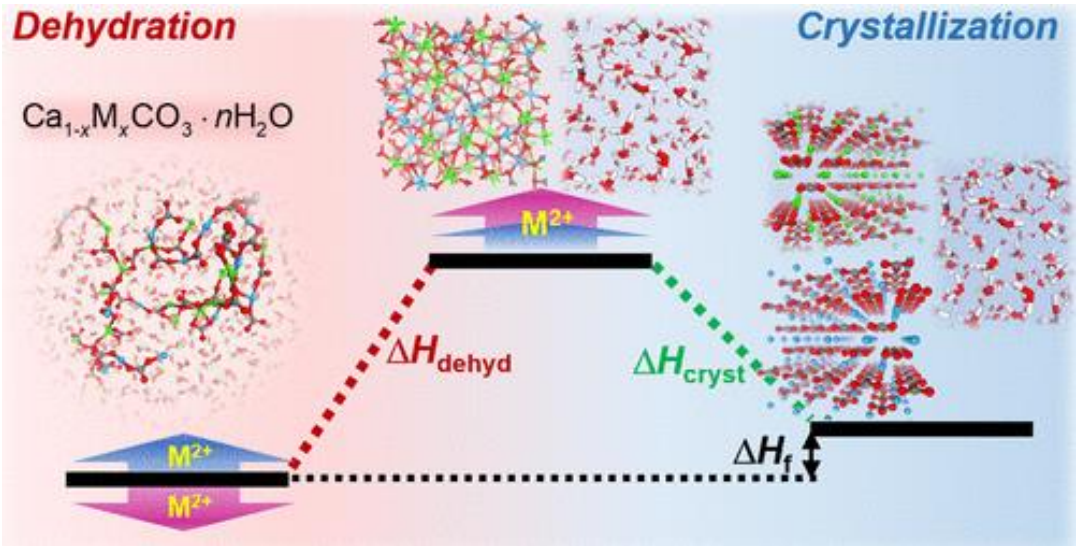

Figure 2.3 Schematic showing dehydration and crystallization of ACC [35]

Bacterial colonization and bacteria-driven infections pose a growing threat against health of individuals. Bacteria are usually apt to gather instead of existing as separate cells. Once bacteria colonize on a surface, they synthesize an organic extracellular matrix layer. This structure is called biofilm, which makes it harder to fight against bacteria and complicates interventional strategies for bacteria related diseases [36], [37]. Furthermore, excessive antibiotic use, along with extraordinary genetic adaptation capability of bacteria led to an uncontrollable increase in the antibiotic resistance strains. In fact, it is estimated that the cumulative loss of economic output due to antimicrobial resistance in the OECD countries will amount to approximately $20-35 trillion by 2050 [38]. Though there are various strategies for sterilization and treatment of bacterial infections, generation of hazardous by-products, cost, toxicity and development of antibiotic resistance are among the problematic issues and lead to eventual abandonment of the utilized antibacterial strategy [39], [40].

Consequently, there is a tremendous need to redesign currently-used disinfection strategies and antibacterial materials [41]. To address the aforementioned challenges, utilization of several alternative antibacterial chemistries, such as carbon-based nanomaterials, silver ions, cationic polymers and selenium nanoparticles, captured a growing interest in the last decade [42], [43].

Selenium (Se) is an essential element for life which involves regulation of cell metabolism for many organisms [44]. It is included in the amino acid selenocysteine (Sec) which eventually forms selenoproteins for various enzymes [45]. Adequate Se intake is crucial for boosting immunity and protection from various diseases, such as thyroid conditions. Se can neutralize the toxic effect of heavy metals like arsenic and lead [46], it has anti-oxidant and anti-cancer properties [47]. In literature, dose dependent antibacterial effect of selenite ions against several bacteria strains, including *Staphylococcus aureus (S. aureus), Escherichia coli (E. coli)* and *Pseudomonas aeruginosa* (*P. aeruginosa),* was verified [48], [49]. In fact, various microorganisms had to take countermeasures for selenium oxyanion toxicity. For instance, *Escherichia coli (E. coli)* reduce selenite to less toxic elemental selenium [50] and transport it outside of their cells. The released elemental selenium accumulates as selenium nanoparticles [51]. Although several types of bacteria can handle selenium and its compounds to some extent, depending on concentration Se exhibits antibacterial activity. Moreover, that the bacteria strains develop a resistance to Se nanoparticles is less likely compared to traditional antibiotics [52].

Utilization of metals and metal oxides to supply bioactive and antibacterial properties is a common approach in the biomaterials field [53]. Magnesium is one of the crucial elements for humans; each adult has an average of 25 g Mg in their body, more than half of it exist in the structure of bone [54]. Mg is responsible for numerous enzymatic reactions as a co-factor [55]. It hinders osteocIast activity and osteolysis, and stimulates formation of bone [56]. It was demonstrated that Mg^{2+} ions combined

with OH^- led to apoptosis of cancerous cells [57]. Aside from magnesium, strontium (Sr) is another vital trace element which is frequently used in orthopedic applications due to its osteoconductive properties [58]. Possessing chemical properties analogous to calcium, Sr can interact with calcium-sensing receptors of osteoblasts, which helps to activate collagen production during bone synthesis. Furthermore, Sr improves osteogenic functions by boosting the release of alkaline phosphatase (ALP) and osteocalcin (OC). Having these properties, Sr is used in osteoporosis treatment [59], [60]. Zinc (Zn) is one of the microelements which participates in cellular components and functioning. Zn does not compromise bone cell functions, and in fact, induce bone cell proliferation [61]. It was demonstrated that zinc dopants not only contributed to bone formation, but also supplied antibacterial activity against *Staphylococcus aureus* (*S. aureus*) and *Escherichia coli* (*E. coli*) [62]. In another study, it was reported that Zn^{2+} ions released from ZnO nanoparticles led to bacterial cell death of Gram-positive, such as *S. aureus, Bacillus cereus* [63], and Gram-negative, such as *E. coli*, *Pseudomonas aeruginosa*, *Salmonella enteritidis*, bacteria strains [64].

In spite of numerous studies investigating the antibacterial properties of metal ions and oxides, the underlying mechanism of action is still not clear. There are various theories suggesting that metallic ions affect bacteria through interaction with nucleic acids, proteins and membranes, which further leads to suppression of the enzymatic and metabolic activities or destruction of the negatively charged cellular membranes [65]. On the other hand, another broad approach claims that metallic ions can play a direct role on production of reactive oxygen species (ROS), which are responsible for antibacterial activity. Despite the fact that ROS at moderate levels can be tolerable by bacteria, extensive ROS generation have destructive effects on cellular functions [66].

CHAPTER 3

EXPERIMENTAL METHODS

3.1 Materials

Calcium acetate monohydrate ($Ca(CH_3CO_2)_2 \cdot H_2O$), sodium bicarbonate ($NaHCO_3$), magnesium chloride hexahydrate ($MgCl_2 \cdot 6H_2O$), sodium selenite (Na_2SeO_3), zinc nitrate hexahydrate ($Zn(NO_3)_2 \cdot 6H_2O$), and strontium chloride hexahydrate ($SrCl_2 \cdot 6H_2O$) were purchased from Sigma Aldrich. Ethylene glycol ($CH_2(OH)_2$) and ethanol (C_2H_5OH) were obtained from ISOLAB Laborgeräte GmbH. Ultrapure water obtained from Millipore Milli-Q purification system was used in the experiments. All chemicals were used as received without further purification.

For biological experiments, Dulbecco's Modified Eagle Medium (DMEM), penicillin-streptomycin, fetal bovine serum (FBS) and trypsin-EDTA were purchased from Biological Industries (BI). 3- (4,5-dimethyl-2-thiazolyl)-2,5-diphenyl-2H-tetrazolium bromide (MTT) was bought from Abcam. Tryptic Soy Broth (TSB) and agar were acquired from Merck.

3.2 Particle Synthesis

ACMC particles were synthesized by co-precipitation method. 5 mL aqueous calcium acetate monohydrate solution (0.5 M) (solution 1), and 5 mL aqueous sodium bicarbonate (0.5 M) and magnesium chloride hexahydrate solution (0.5 M) (solution 2) were prepared separately in different beakers. Then, the total volume of each beaker was adjusted to 25 mL by ethylene glycol. Calcium acetate solution was poured into the sodium bicarbonate-magnesium chloride solution. The reaction took place for 15 min under magnetic stirring, and afterwards the solution was kept stationary for 1 h. The precipitate was isolated from supernatant by centrifugation,

and then washed with ethanol and ultrapure water, respectively. Lastly, the powder was lyophilized to remove excess water. The experiments were conducted at room temperature. For the production of ion incorporated particles, the same protocol was followed, except further addition of sodium selenite at 0.001, 0.005 and 0.01 M concentrations to sodium bicarbonate and magnesium chloride hexahydrate solution for selenite incorporated particles; and further addition of zinc nitrate hexahydrate (0.01 and 0.1 M) and strontium chloride hexahydrate (0.01 and 0.1 M) to calcium acetate monohydrate solution for zinc and strontium incorporated particles prior to mixing solution 1 and 2. Molarity values of the precursor salts in 5mL ultrapure water are given in Table 3.1 for Chapter 4 and in Table 3.2 for Chapter 5.

Table 3.1 Molarity of the precursor solutions prepared for selenite incorporated particles

Sample Designations	**Solution A**	**Solution B**		
	$Ca(CH_3CO_2)_2 \cdot H_2O$ (M)	**$NaHCO_3$ (M)**	**$MgCl_2 \cdot 6H_2O$ (M)**	**Na_2SeO_3 (M)**
ACMC	0.5	0.5	0.5	-
Se(I)-ACMC	0.5	0.5	0.5	0.001
Se(II)-ACMC	0.5	0.5	0.5	0.005
Se(III)-ACMC	0.5	0.5	0.5	0.01

Table 3.2 Molarity of the precursor solutions prepared for zinc and strontium incorporated particles

Sample Designations	**Solution A**			**Solution B**	
	$Ca(CH_3CO_2)_2 \cdot H_2O$ (M)	**$Zn(NO_3)_2 \cdot 6H_2O$ (M)**	**$SrCl_2 \cdot 6H_2O$ (M)**	**$NaHCO_3$ (M)**	**$MgCl_2 \cdot 6H_2O$ (M)**
ACMC	0.5	-	-	0.5	0.5
ZA-1	0.5	0.01	-	0.5	0.5
ZA-2	0.5	0.1	-	0.5	0.5
ZSA-1	0.5	0.01	0.01	0.5	0.5
ZSA-2	0.5	0.1	0.1	0.5	0.5

3.3 Particle Characterization

3.3.1 Scanning Electron Microscopy (SEM)

The morphology of the ACMC nanoparticles were observed using scanning electron microscopy (SEM, FEI Nova Nano SEM 430). 15 kV accelerating voltage was used to capture SEM images. Prior to imaging, ACMC particles were coated with gold using Quorum SC 7640 high resolution sputter coater.

3.3.2 Energy Dispersive Spectroscopy (EDS)

Elemental composition of the synthesized nanoparticles was determined by energy dispersive X-ray spectroscopy (EDS) technique. The presence of the incorporated ions inside the nanoparticles was confirmed using EDS.

3.3.3 Transmission Electron Microscopy (TEM)

Amorphous structure was substantiated by high resolution transmission electron microscopy (JEOL JEM - 2100F). The nanoparticles were prepared in 99% ethanol and dried on carbon-coated copper TEM grids prior to imaging.

3.3.4 X-ray Diffraction (XRD)

To demonstrate the amorphous nature of synthesized nanoparticles, X-Ray diffraction (XRD) analyses were performed with Rigaku D/Max - 2200 X-Ray diffractometer with monochromatic Cu Kα radiation (λ=1.54 A°) at 2 °/min scanning rate between 20° - 60°.

3.3.5 X-Ray Photoelectron Spectroscopy (XPS)

To analyze the chemical composition of the nanoparticles and to assess the chemical state of selenium, X-Ray Photoelectron Spectrometer (XPS) analysis was conducted using Kratos Analytical Axis Supra having a monochromatic Al Kα (1486.7 eV) excitation source. All spectra were calibrated according to the adventitious carbon peak at 284.8 eV, and then fitted using CasaXPS software. The National Institute of Standards and Technology XPS Online database was used to interpret the XPS data and to determine the binding energies.

3.3.6 Fourier Transform Infrared Spectrometer (FTIR)

To determine the chemical bonding of the nanoparticles, Fourier transform infrared spectroscopy analyses were carried out using Perkin Elmer Spectrum 100 in ATR mode, and the samples were scanned in 4000 - 400 cm^{-1} range. Characteristic absorption bands were used for the identification of the nanoparticles.

3.3.7 Thermogravimetric Analysis (TGA)

Thermogravimetric analyses were performed with SDT 650 in nitrogen atmosphere between 25 - 800 °C temperature range with a heating rate of 10 °C/min to examine the thermal characteristic of the samples. Thermal stability and water content was calculated from the obtained TGA curves.

3.3.8 Degradation Test

Degradation tests were conducted in phosphate buffer solution (1xPBS). Nanoparticles were added into 1xPBS at 1 g/L of concentration and kept at 37 °C through the degradation experiments. pH of the solutions was measured at 1 min, 5 min, 15 min, 1 h, 24 h, 48 h, and 72 h time periods.

3.4 Biological Experiments

3.4.1 Particle Extraction

Prior to viability tests, nanoparticles were sterilized under UV light for 1 h. Afterwards, specimens were extracted using culture media at a concentration of 1 g/L for selenite incorporated nanoparticles and 0.01 g/L for zinc and strontium incorporated nanoparticles at 37 °C for 72 h. The culture media used for the extractions were 0.3% tryptone soy broth (TSB) for the antibacterial activity tests and growth medium for the cell viability assay. After extracting the nanoparticles inside the aforementioned media for 72 h at 37 °C, the supernatant was separated by centrifugation and the extracted media were used for the biological experiments.

3.4.2 Cell Viability Assay

Cell Culture

L929 fibroblast cells (ATCC# CCL-1) were used to assess cellular viability (cytotoxicity). Dulbecco's Modified Eagle Medium (DMEM, Sigma Aldrich) supplemented with 1% penicillin/streptomycin and 10% fetal bovine serum (FBS) was used as the growth medium. Fibroblasts were kept in a humidified 5% CO_2 incubator at 37 °C and passaged at 90% confluency every 2 to 3 days.

Cell Viability Assay

The experiments were performed in a laminar flow hood to retain sterile conditions. For viability experiments, fibroblasts were seeded into 96-well plate at a concentration of 1 x 10^4 cells per well using the growth medium. After 24 h, the media were replaced with 200 µl of specimen extracts. At the 1^{st}, 3^{rd} and 5^{th} days of incubation MTT 3 - (4,5 – dimethyl – 2 - thiazolyl) - 2,5 – diphenyl - 2H - tetrazolium bromide) assay was carried out. Each well was rinsed with 1xPBS and 125 µl of 1

g/L sterilized MTT solution (Sigma Aldrich) was added into each well. 4 h later, the formed formazan crystals were dissolved with 0.77% HCl 2 - isopropanol solution (1:1 volume ratio). The absorbance values were measured at 570 nm using Thermo Scientific Multiskan Go microplate spectrophotometer (Waltham, Massachusetts). A cell free well was used to obtain the absorbance of the blank sample and its absorbance value was subtracted from the obtained absorbance values. Cells which were not treated with calcium carbonate extracts were used as control.

3.4.3 Antibacterial Activity Tests

ACMC nanoparticles were tested against two different Gram-positive bacteria: *Staphylococcus aureus* (ATCC# 25923) and *Staphylococcus epidermidis* (ATCC# 35984); and two different Gram-negative bacteria: *Escherichia coli* (ATCC# 10536) and *Pseudomonas aeruginosa* (ATCC# 27853).

Bacteria from stock culture were inoculated onto LB agar plates, and incubated overnight. Once the colonies grew, a single colony forming unit (CFU) was isolated and inoculated in 3% tryptone soy broth (TSB). Afterwards, it was cultured inside a shaking incubator at 37 °C and 200 rpm for 18 h. At the end of 18 h, bacteria were diluted to an optical density of 0.01 at 625 nm (OD_{625}), which was further diluted 1:100 with 1xPBS. 100 µl of suspended bacteria were seeded into 96-well plates at a density of $ax10^5$/mL (a=4, 9, 8, 5 for *S. aureus, S. epidermidis, E. coli* and *P. aeruginosa,* respectively). 100 µl of nanoparticle extracts were also added into each well to make the total volume 200 µL/well. After 24 h of incubation, the bacteria in the wells were serially diluted with 1xPBS, and 20 µl of the dilution were seeded onto agar plates to observe individual colonies. Lastly, agar plates were incubated overnight at 37 °C to count for CFUs.

3.4.4 Statistical Analysis

All the biological experiments were repeated three times and three samples were used for each experiment. The results were reported as mean ± standard deviation. One-way ANOVA method with Tukey's post hoc test was used to determine whether the data showed a meaningful statistical difference. Statistical significance was fixed at $p < 0.05$.

CHAPTER 4

SELENITE INCORPORATED ACMC

4.1 Results and Discussion

4.1.1 Synthesis and Characterization of Nanoparticles

Amorphous nanoparticles were synthesized through bottom-up route and stabilized in the presence of Mg^{2+} ions. Aqueous EG solution of calcium acetate monohydrate (solution 1) and sodium bicarbonate and magnesium chloride hexahydrate (solution 2) were prepared separately. Then, solution 1 was poured into solution 2 to initiate precipitation reaction. SeO_3^{2-} ion incorporation was done via co-precipitation technique. The same protocol was followed except that sodium selenite was added to sodium bicarbonate and magnesium chloride hexahydrate solution prior to the mix of solutions. Three different concentrations of SeO_3^{2-} were incorporated (Se(a)-ACMC) as 0.001, 0.005 and 0.01 M. In Figure 4.1a synthesis schematic and sample naming are shown.

SEM images illustrate the homogeneously distributed agglomerated nanoparticle morphology (Figure 4.1b-e). After selenite incorporation, there was no sign of a notable secondary morphology. Similarly, the increment in the selenite amount did not cause any change in the particle morphology.

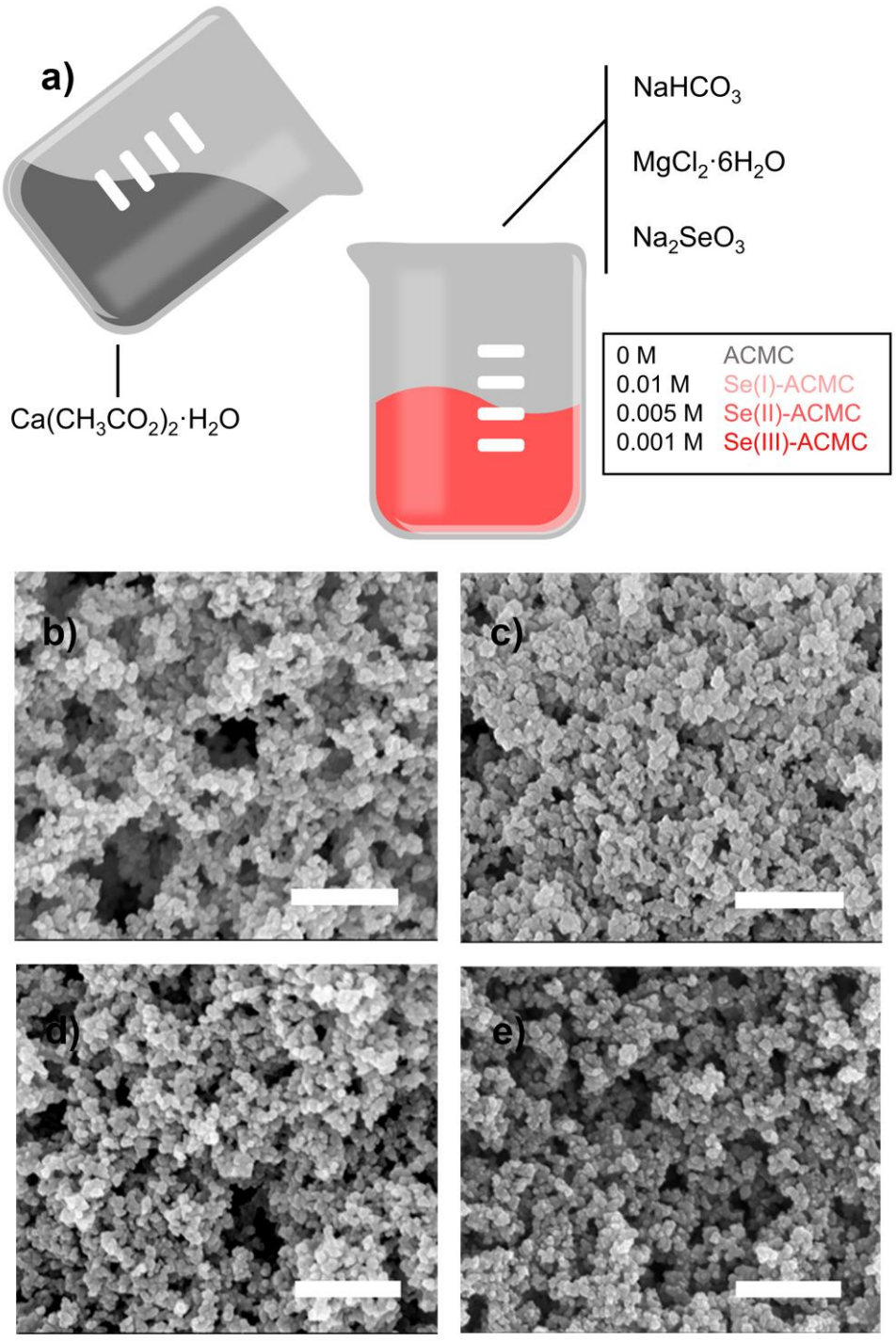

Figure 4.1 a) Sketch showing the synthesis protocol for the nanoparticles. (b-e) SEM images of b) ACMC, c) Se(I)-ACMC, d) Se(II)-ACMC and e) Se(III)-ACMC nanoparticles, scale bars are 500 nm.

The bumps in the XRD analysis revealed the amorphous structure of the nanoparticles and lack of any major secondary crystalline phase (Figure 4.2c). TEM characterization was conducted for ACMC and the highest SeO_3^{2-} concentration (Se(III)-ACMC) to confirm the amorphous bumps of the XRD results. The rings in the SAED pattern validated the amorphous nature of the particles; there was no crystallization after selenite incorporation (Figure 4.2a,b).

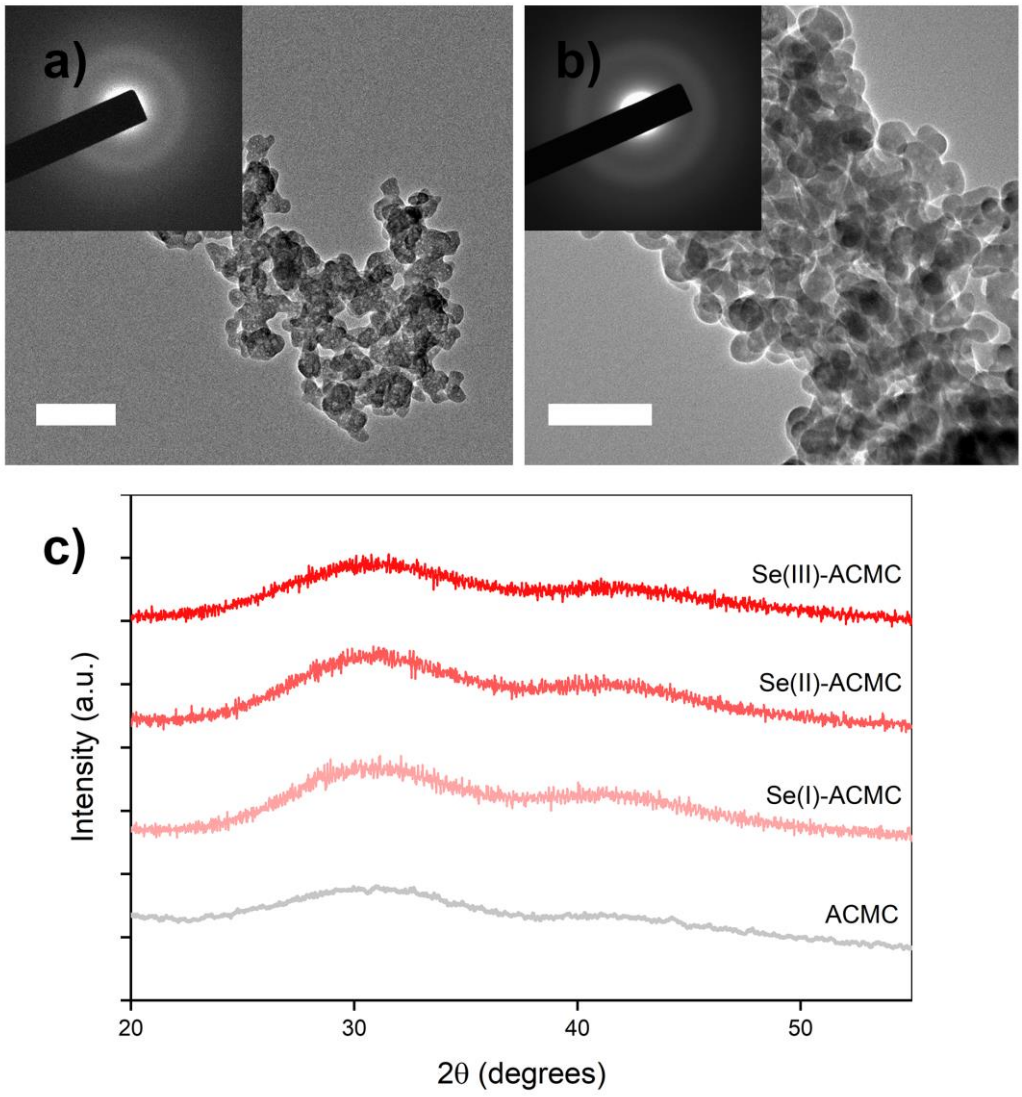

Figure 4.2 (a-b) TEM images and SAED patterns of a) ACMC and b) Se(III)-ACMC, scale bars are 100 nm. c) XRD patterns of the samples.

In Figure 4.3, average particle sizes of the nanoparticles are exhibited. The average particle size of ACMC was found as 34.2. The measurements indicated that selenite ions did not cause an alteration in the particle size.

Samples	Particle Size (nm)
ACMC	34.2 ± 6.1
Se(I)-ACMC	34.5 ± 5.7
Se(II)-ACMC	35.3 ± 5.7
Se(III)-ACMC	33.6 ± 7.7

Figure 4.3 Particle size measurement of nanoparticles

FTIR was used to investigate the chemical composition of the synthesized nanoparticles. In Figure 4.4a, the characteristic carbonate bands of ACC are presented. That all the bands widened implied a less definite arrangement. The symmetric stretching band at ~ 1084 cm^{-1} (υ_1), the out of plane band at ~ 859 cm^{-1} (υ_2), the asymmetric stretching band at 1412 & 1477 cm^{-1} (υ_3) and in-plane deformation band at around 688 & 728 cm^{-1} (υ_4), are associated with the carbonate ions in ACC. Furthermore, the lack of the calcite peak at 718, vaterite peak at 745 and aragonite peaks at 700 and 712 proved that crystallization did not occur [67]. Compared to ACMC, for Se-ACMC particles, there was a gradual increase in the intensity of the band at ~ 770 cm^{-1} depending on the rise in selenite quantity. It could be ascribed to Se-O bending vibrations [68] of selenite based on the high intensity band at similar region for sodium selenite. The wide band at 3400 cm^{-1} and the small band at 1640 cm^{-1} were attributed to

O-H bonding; stretching and bending vibrations of water, which could stem from the physically and chemically bonded water and hydroxide ions in the molecule.

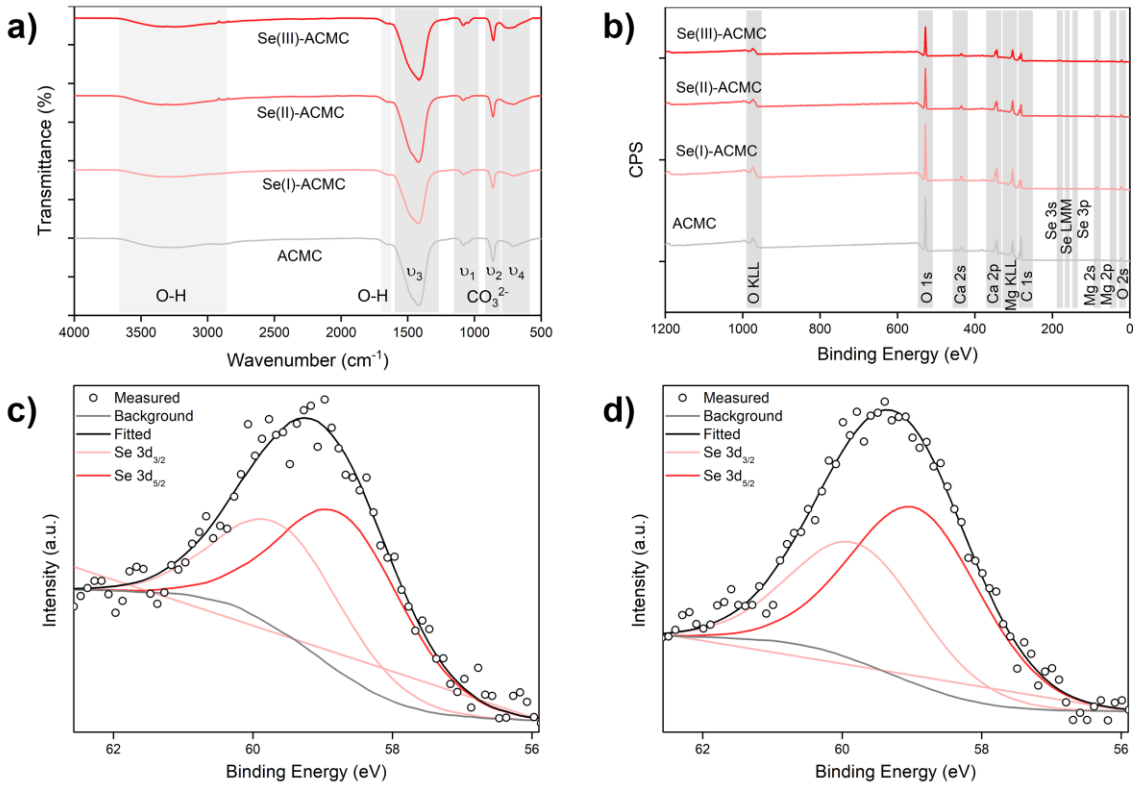

Figure 4.4 a) FTIR and b) wide-scan XPS spectra of the samples. (c-d) High resolution XPS spectra of c) Se(II)-ACMC and d) Se(III)- ACMC nanoparticles.

Survey spectra of XPS showed the elemental composition of the mineralized nanoparticles (Figure 4.4b). The presence of calcium, magnesium, carbon and oxygen elements in all of the samples, and selenium in Se-ACMC nanoparticles were verified. High resolution scan of the 3d core level of Se was done to determine the oxidation state of selenium. The binding energies of $Se3d_{5/2}$ and $Se3d_{3/2}$ were found by deconvolution of peaks using the CasaXPS program. Depending on increased selenite quantity, intensity of the peaks rose. Because the peak intensity of Se3d was not high enough, the deconvolution process was not applied to Se(I)-ACMC. Peak fitting was done choosing

Shirley background using the combination of Gaussian and Lorentzian functions, and putting constraints on peak area ratio and peak positions. According to the National Institute of Standards and Technology (NIST) database, the binding energy of $Se3d_{5/2}$ for Se(IV) is between 58.8 and 59.9. In the analysis, the peak separation between $Se3d_{5/2}$ and $Se3d_{3/2}$ was restricted to 0.86 eV, as given in the NIST database. Based on basic XPS knowledge, peak area ratio for d orbitals was set as 3/2. Consequently, the binding energy of $Se3d_{5/2}$ was found as 58.97 for Se(II)-ACMC, and 59.10 for Se(III)-ACMC. Hence, the charge of selenium was determined as Se(IV) or Se^{4+} (selenite), which was consistent with the NIST database. As a result, XPS high resolution spectrum justified the existence of selenite ions in the structure.

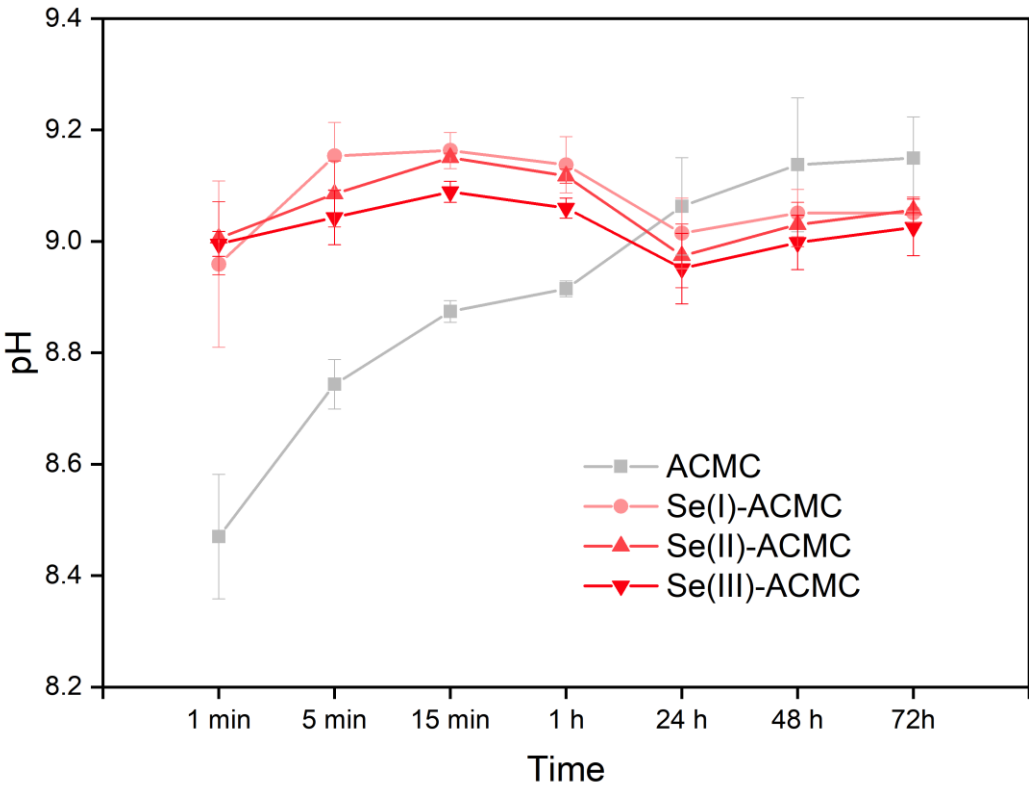

Figure 4.5 Degradation result of the nanoparticles in 1x PBS up to 72.

Degradation test was performed measuring the pH values of samples in PBS with a pH of 7.4 (Figure 4.5). Ion dissociation caused pH change resting on CO_3^{2-} release. To determine the contribution of selenite ions to pH, equal molar (0.01 M) of sodium bicarbonate and sodium selenite salts were dissolved in ultrapure water and pH values were recorded as 8.63 and 9.56, respectively. However, because the molarity was far less than carbonate, the main contribution was expected from CO_3^{2-}. The results showed that there was a sudden release of ions within minutes. From 24 h onward, ion release went on at a diminishing rate. After selenite substitution, the initial value of pH increased fairly, which most probably indicated that Se-ACMC nanoparticles released carbonate more than ACMC; in other words, degraded faster. Moreover, results showed that from the first moment degradation occurred. In the stabilization of ACC, the role of Mg^{2+} ions in the solution is significant since they can act as barriers to calcite nucleation obstructing calcite nucleation sites [69]. Therefore, fast dissolution kinetics in aqueous medium could stem from the lack of ions that could create a barrier to ion mobility. Degradation results also signaled a decrease in the degradation rate after 24 h, which was most probably due to the crystallization of the ACMC nanoparticles since the degradability of amorphous phase is higher than crystalline polymorphs.

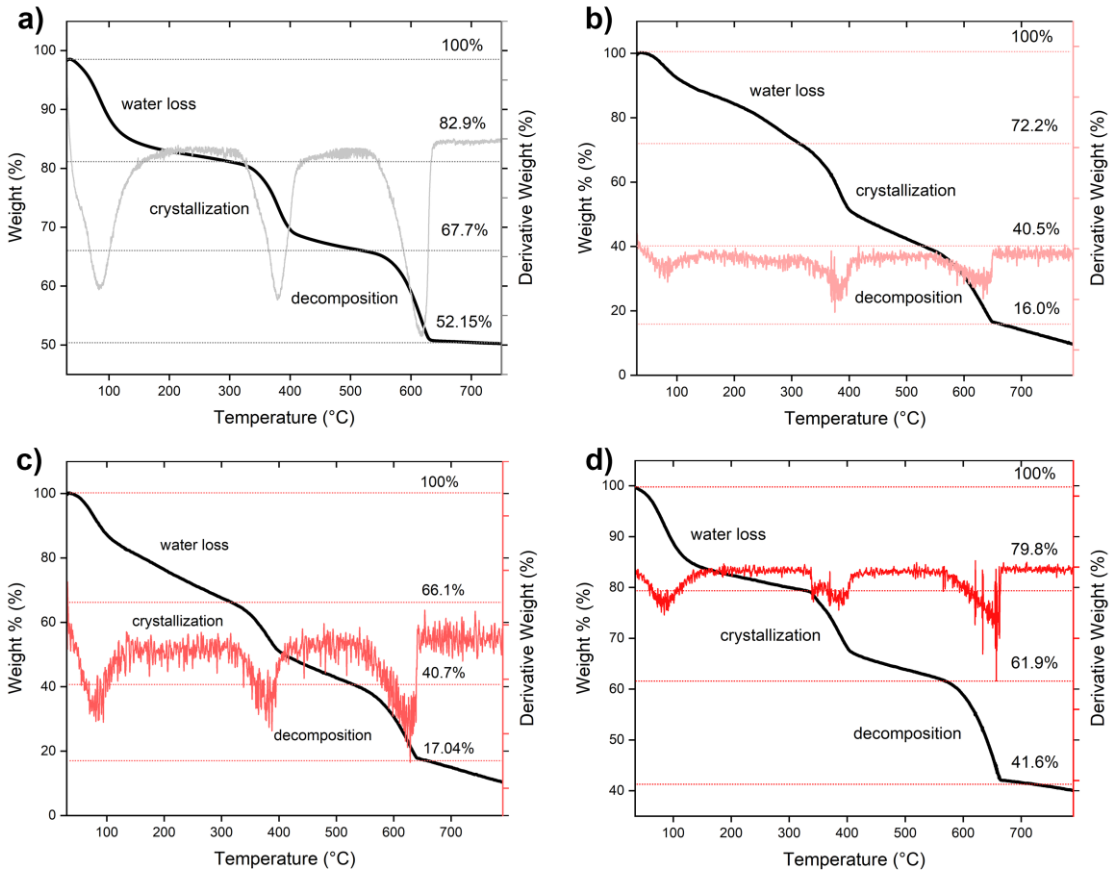

Figure 4.6 (a-d) TG analysis showing mass loss and derivative of the mass loss curves for a) ACMC, b) Se(I)-ACMC, c) Se(II)-ACMC and d) Se(III)- ACMC nanoparticles.

Thermal stability and water fraction was determined by TG analysis (Figure 4.6). The TGA curve of ACMC nanoparticles exhibited three major mass loss events heating up to 800 °C. The first one was ascribed to water removal. In Se-ACMC samples, the water content mounted compared to ACMC. While ACMC included ~17% of structural water, Se(I)-ACMC and Se(II)-ACMC had ~28% and ~33%, respectively. For Se(III)-ACMC water fraction was reduced to 20%, which was still higher than ACMC. When the degradation result and TGA results are interpreted together, it could be contemplated that selenite ions in the structure caused an increase in the water content, which increased the ion mobility in bulk water and consequently dissolution.

An increase in the crystallization temperature meant that thermal stability increased. Because there was not a significant alteration at the onset of the crystallization temperature, it could be deduced that selenite ions did not affect thermodynamic stability. The second mass loss curves of Se-ACMC nanoparticles involved two events with overlapping temperatures. This might be due to phase separation during crystallization. Selenite may not be compatible with magnesian calcite.

4.1.2 Antibacterial Performance

To evaluate the antibacterial activity of the particles CFU Assay was conducted. CFU per mL graphs are shown in Fig 3.4. The middle selenium concentration (Se(II)-ACMC) and control sample were photographed to show the decrease in CFU. A decrease in the number of micro-colonies on the agar plates compared to bacterium control sample directly affirmed the antibacterial activity. The results indicated that after 24 h of contact with bacteria ACMC particles showed no antibacterial effect against bacteria except for *S. epidermidis*, whereas the selenite incorporated particles rendered all four types of bacteria ineffective. Increasing selenite concentration (from Se(I)-ACMC to Se(III)-ACMC) enhanced the effectiveness in handling the bacteria. For *S. aureus* there were 81%, 77% and 87% decrease in CFU/mL values of Se(I)-ACMC, Se(II)-ACMC and Se(III)-ACMC, respectively with respect to control. For *S. epidermidis*, ACMC reduced CFU/mL by 85%, and the rest of them by about 99.9%. For *E. coli* Se(I)-ACMC, Se(II)-ACMC and Se(III)-ACMC reduced bacteria by 30%, 30 % and 60%, respectively. Lastly, for *P. aeruginosa* there was a 27%, 38% and 80% decrease as a result of the exposure to Se(I)-ACMC, Se(II)-ACMC and Se(III)-ACMC. Antibacterial activity of selenite ions on Gram-positive bacteria (*S. aureus, S. epidermidis*) was far more prominent than the Gram-negative bacteria (*E. coli, P. aeruginosa*).

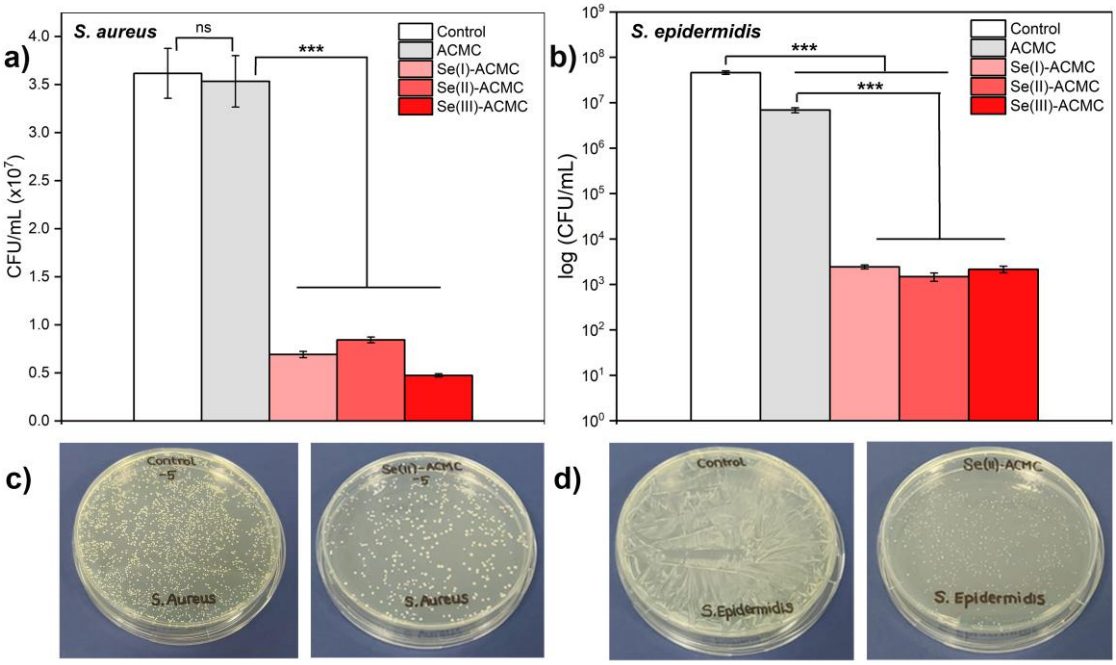

Figure 4.7 Antibacterial activity of the nanoparticles against gram positive bacteria strains as a) and c) *S. aureus*, b) and d) *S. epidermidis*. c) and d) Photographs of the agar plates showing the differences in CFUs upon the interaction with the nanoparticles.

Moreover, after 24 h incubation, in extract Se-ACMC samples, red-orange color was observed. Depending on the reduction of selenium oxyanions to elemental form, a reddish color is reflected [70]. It has been reported that this color change is an indicator for the involvement of bacteria in reduction of selenite [71]. It is known that elemental selenium has far less toxicity than selenite and selenite which are reduced by the bacteria' enzymes so the detrimental effect on nature can be undermined [51].

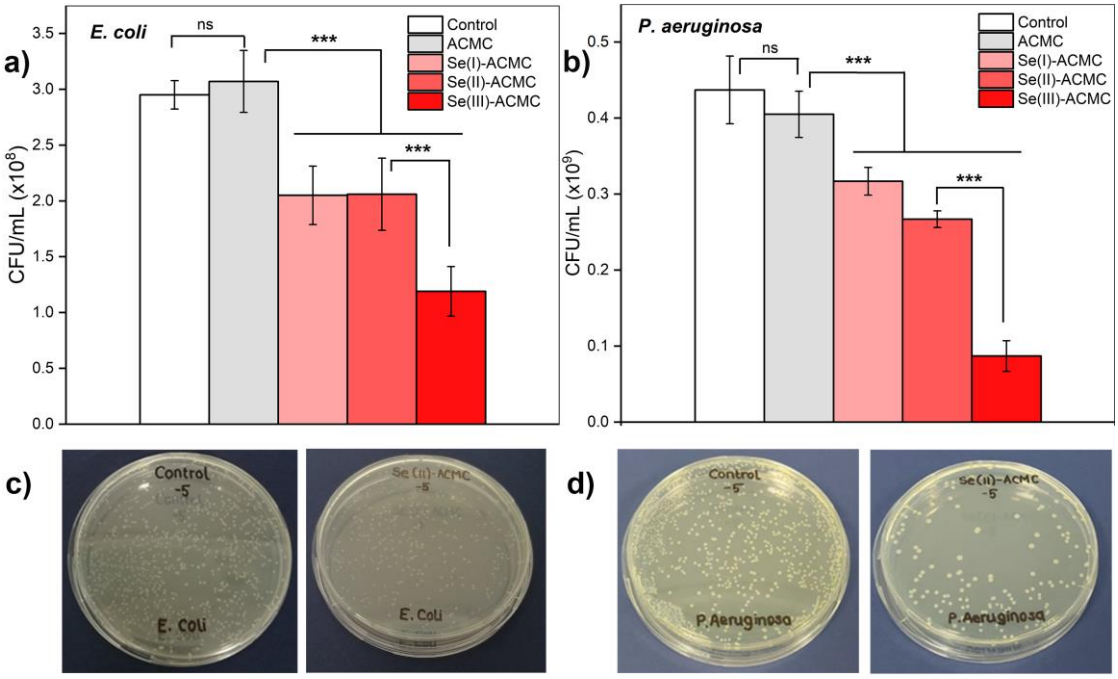

Figure 4.8 Antibacterial activity of the nanoparticles against a) and c) *E. coli*, b) and d) *P. aeruginosa*. c) and d) Photographs of the agar plates showing the differences in CFUs upon the interaction with the nanoparticles.

CHAPTER 5

ZINC AND STRONTIUM INCORPORATED ACMC

5.1 Results and Discussion

5.1.1 Particle Synthesis and Characterization

In this chapter, I proposed Zn^{2+} and/or Sr^{2+} incorporated Mg^{2+} stabilized amorphous calcium carbonate to be used for biomedical applications owing to its biocompatibility, biodegradability and consisting of ions which are also present in the human body. For instance, it could be utilized as a bone reconstruction material when constituents of ACMC were taken into consideration. As a calcium source, due to higher solubility than other calcium compounds it could make a rapid Ca^{2+} contribution to the region. It was frequently acknowledged that osteoclast activation was induced by the released phosphate radicals, which intensified the acidity of the environment [72]. For those reasons ACMC nanoparticles could be favorable during bone healing process. Moreover, as a matter of fact, each crystalline biomineral evolved from an amorphous form. For instance, bone apatite formation involves step-wise transitions from ACC to ACP, and eventually HAp [73]. Alternatively, these nanoparticles could be designed as the bioceramic part of a drug carrier. pH-responsive biodegradability and high loading capacity stemming from its nano size could make ACMC nanoparticles a promising drug carrier candidate.

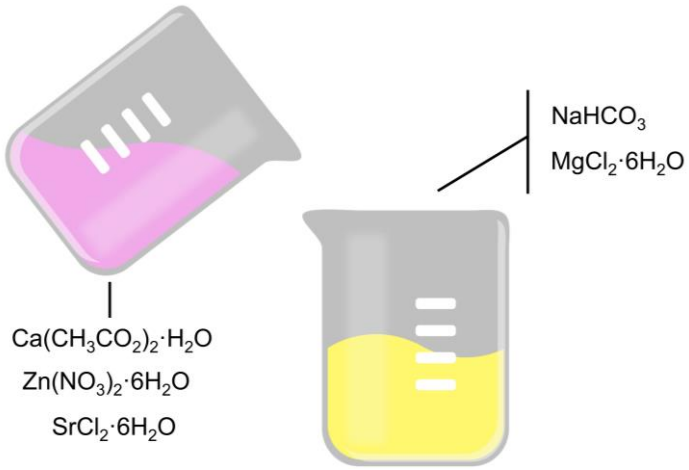

Figure 5.1 Sketch showing the synthesis protocol for the nanoparticles.

Bacteria-related complications pose a serious challenge to the medical field. Utilization of nanomaterials can be a feasible solution. Although ACMC itself did not have an antibacterial activity, its nature made it possible to insert several ions into its structure. In literature it was validated that zinc ions had antibacterial characteristics and, both zinc and strontium have advantages for humans such as enhancing bone formation and hinder bone resorption [74]. Therefore, substitution of those ions could improve the material in several aspects. In literature, hydroxyapatite was co-substituted with strontium and zinc ions [75]. However, there was no study that ACC or ACMC was co-incorporated with Zn^{2+} and Sr^{2+}. The reason why bivalent ions such as Zn^{2+} and Sr^{2+} were successfully used as dopants in HAp was that Ca^{2+} could be readily displaced by those ions with similar ionic radii [76]. Similarly, those ions could be replaced by Ca^{2+} in $CaCO_3$ structure. Hence, Zn^{2+} and Sr^{2+} co-substituted ACMC nanoparticles can be produced via a simple wet chemistry technique, which is shown in Figure 5.1.

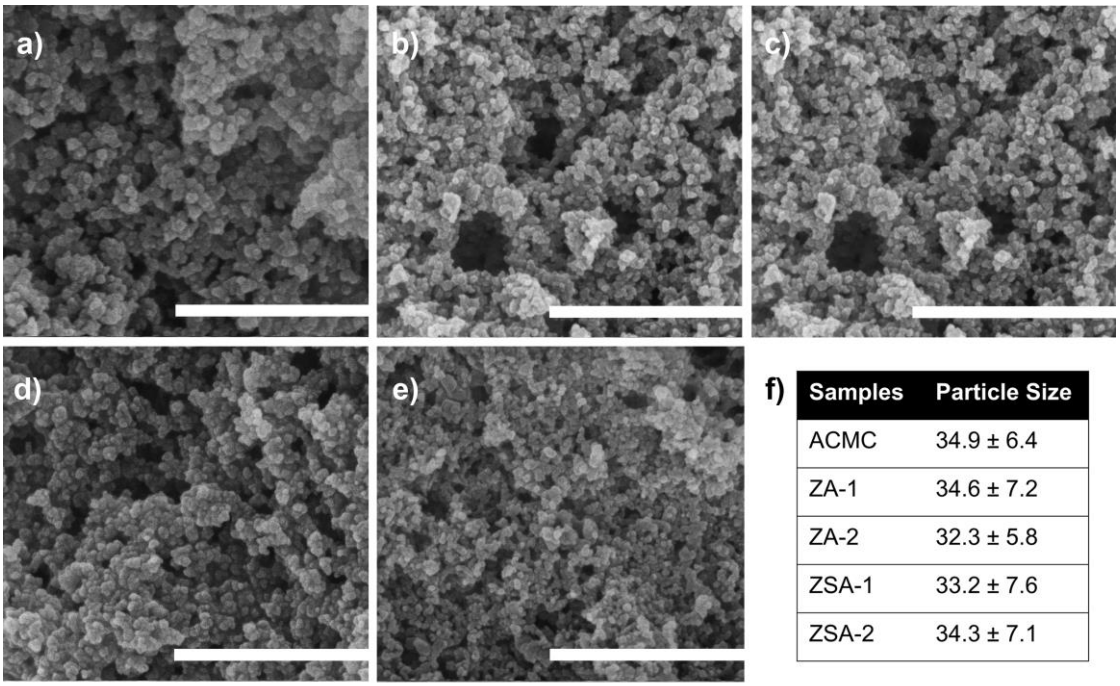

f)

Samples	Particle Size
ACMC	34.9 ± 6.4
ZA-1	34.6 ± 7.2
ZA-2	32.3 ± 5.8
ZSA-1	33.2 ± 7.6
ZSA-2	34.3 ± 7.1

Figure 5.2 a), b), c), d), and e) SEM images of a) ACMC, b) ZA-1, c) ZA-2, d) ZSA-1 and e) ZSA-2 nanoparticles. f) Particle size measurement in nm unit.

Zinc and strontium substituted nanoparticles were produced through co-precipitation. Calcium acetate monohydrate, zinc nitrate hexahydrate and strontium chloride hexahydrate salts (A) and sodium bicarbonate, magnesium chloride hexahydrate salts (B) were dissolved in 80% of aqueous ethylene glycol, separately. Later, solution A was added to solution B. The reaction took place for 15 min under magnetic stirring and 1 h being kept stationary. For ZA-1 and ZA-2 samples, strontium chloride hexahydrate was excluded.

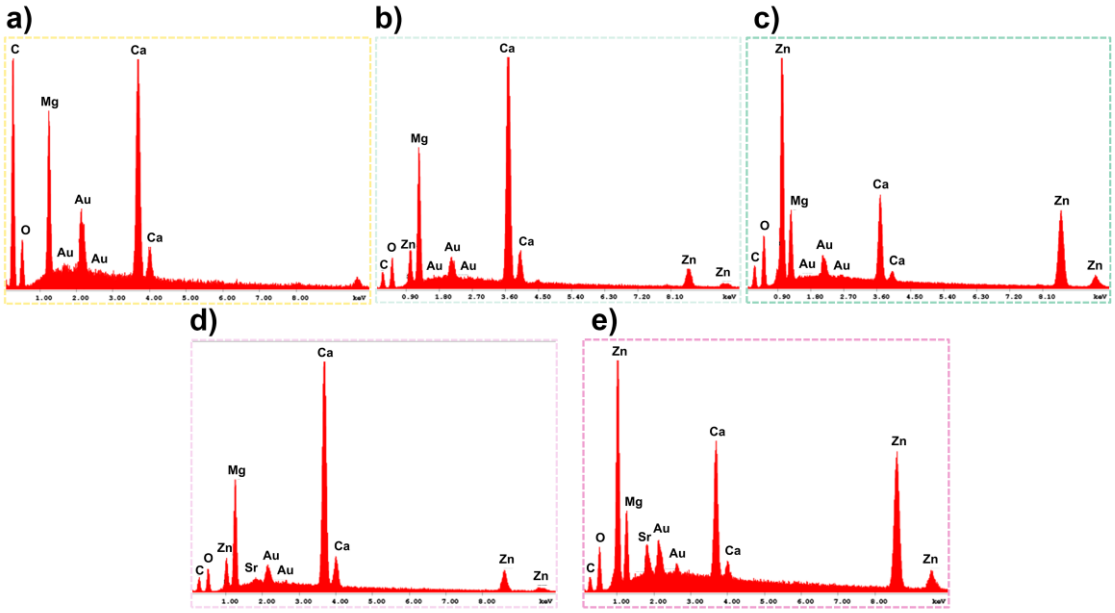

Figure 5.3 a), b), c), d), and e) EDS graphs of d) ACMC, b) ZA-1, c) ZA-2, d) ZSA-1 and e) ZSA-2 nanoparticles.

Nanostructure of the particles were displayed in Figure 5.2a-e. ACMC nanoparticles had typical agglomerated nano-sized morphology, and substitution of Zn and Sr did not result in the formation of a secondary morphology. In Figure 5.2f, average particle size values of the nanoparticles are given. The average particle size of ACMC was measured 34.9 nm, and after Zn and Sr ion incorporation consequent average particle size remained at a similar range. EDS graphs in Fig 5.3 show the elemental composition of the samples. The existence of Zn and Sr in the structure was affirmed. The amorphous humps and lack of any sharp diffraction peaks in the XRD graph (Figure 5.4a) proved the amorphous nature of the nanoparticles. Furthermore, that technique confirmed that no notable secondary phase crystallized.

FTIR result is presented in Figure 5.4b. The wide band at ~3400 and ~1640 the small band at are associated with O-H bond, which can stem from water molecules and

hydroxyl ions. The characteristic carbonate bands in the fingerprint region are shown in the dark area. The bands at ~705, ~860, ~1084 and ~1417-1467 represented in plane bending, out of plane bending, symmetric stretching and asymmetric stretching vibrational modes, respectively [19]. The lack of some of the characteristic bands for $ZnCO_3$ at ~1046, ~1383 and ~1511 [77] and for $SrCO_3$ at 1070, 1771 [78] indicated that neither $ZnCO_3$ nor $SrCO_3$ crystallized during synthesis.

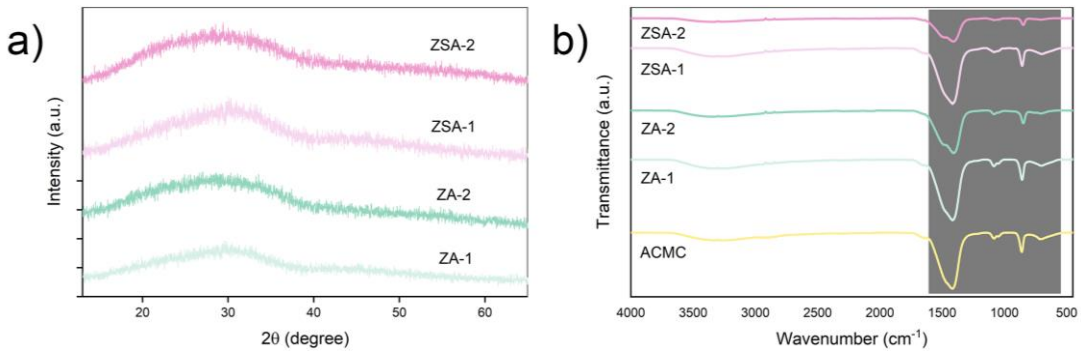

Figure 5.4 a) XRD and b) FTIR test results of nanoparticles.

Degradation performance was assessed by measuring pH values of nanoparticles prepared in PBS medium (Figure 5.5). An increase in the pH was directly proportional to CO_3^{2-} ion release. The graph indicated that from the first moment ion release started. The pH values were recorded for three days and ion release continued along the way. After substitution of Zn and Sr at lower concentrations (ZA-1 and ZSA-1), there was not a significant change in the degradation behavior; however, at higher concentrations (ZA-2 and ZSA-2), pH values were less alkaline compared to the former ones, meaning that ion release was reduced. Composition of the nanoparticles changed the degradation performance. The reason for more alkaline pH signifying more CO_3^{2-} released, or faster degradation could be correlated to kinetic stability of the nanoparticles. The results indicated that the nanoparticles began to degrade from the first moment. The fast degradation kinetics could be ascribed to lack of free Mg^{2+} ions in the medium, which hindered calcite crystallization during ACC or ACMC dissolution [69]. Moreover, Zn

and Zn/Sr together at high concentrations decreased the initial degradation rate. In literature, via MD simulations it was explained that ionic additives affected the stability of ACC depending on their several properties such as ionic radius and hydrophilicity. Whereas smaller and more hydrophilic Mg ions hamper the crystallization of ACC, larger and less hydrophilic Sr accelerates it [35]. Based on that study, Zinc might have a crystallization hampering effect at high concentration.

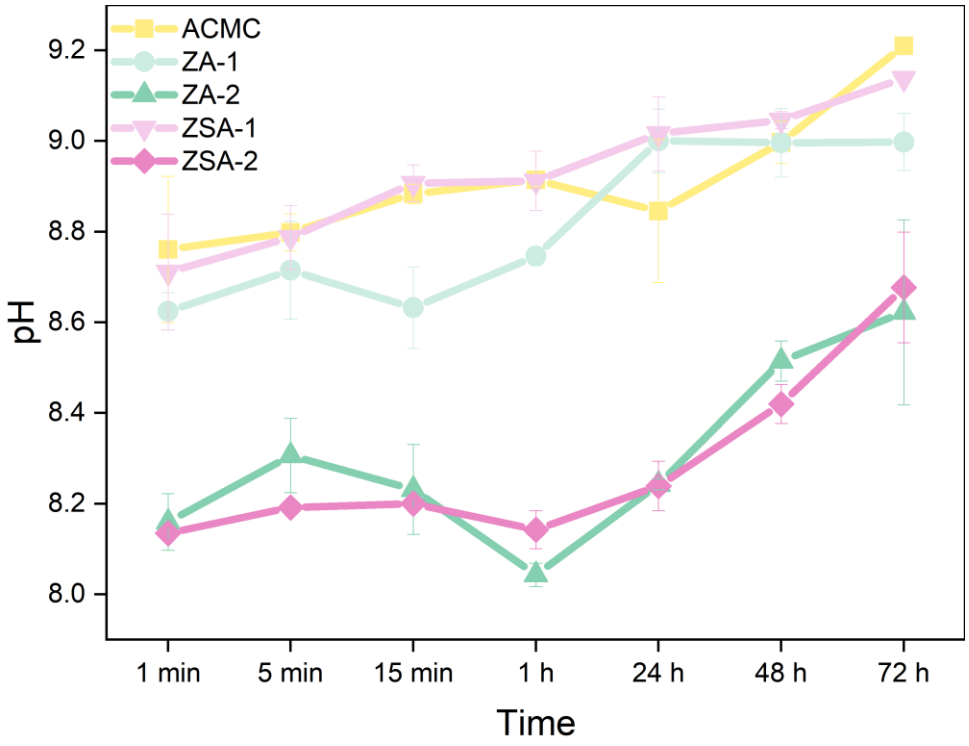

Figure 5.5 Degradation test results of nanoparticles.

In Figure 5.6, TG analysis results of the nanoparticles are illustrated. Three main events in TGA graphs were classified as water loss, crystallization and decomposition to CaO and MgO. That there was not a substantial change in the crystallization temperature showed that those ions did not affect the thermal stability. Water content of the nanoparticles is exhibited in the graphs as percentage. ACMC, ZA-1 and ZSA-1 particles had 17%, 22% and 22% respectively. On the other hand, at higher ion

concentration, for ZA-2 and ZSA-2, water amount was measured as 19% and 14%, respectively.

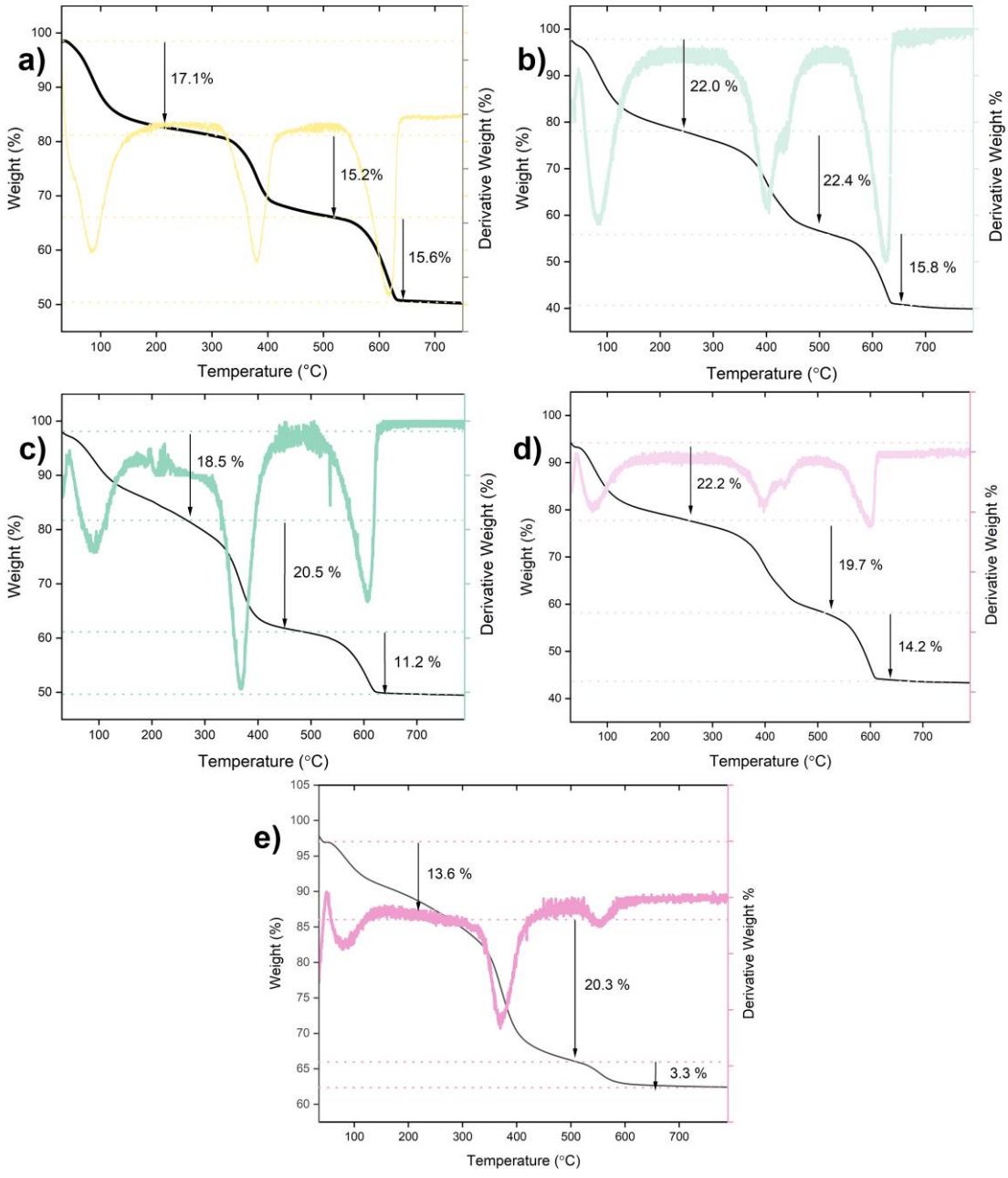

Figure 5.6 (a-e) TG analysis showing mass loss and derivative of mass loss curves for a) ACMC, b) ZA-1, c) ZA-2, d) ZSA-1 and e) ZSA-2.

According to the TGA curves, there was a slight increase in water content depending on ion substitution. Physically bonded water is eliminated up to around 120 °C, and the amount can differ independently of the type of sample [79]. Rest of the water, namely structural water, is excluded simultaneously with crystallization of ACMC [10]. Inorganic additives change ion mobility forming bonds with one or more of calcium, water and hydroxyl ions [20]. According to the degradation result it is likely that water content did not make the main contribution. Zinc ions at high concentration (0.1 M) could be the main reason for reduced degradation pace.

5.1.1.1 Cell Viability

Zn^{2+} is one of the transition metal ions whose massive accumulation causes toxicity to biological organisms. On the other hand, a complex physiological environment restrains antibacterial activity of the ions. Hence, it is critical to achieve the balance between non-toxicity and antibacterial effect by preparation and stabilization techniques [80]. Cell viability assay was conducted to determine whether the nanoparticles were cytotoxic. The working principle of the assay depended on formazan crystals that were transformed from MTT by only living and healthy cells, which were the direct indicator of cell viability. In this research, we pick L929 cell line to assess cytotoxicity. For each sample cell viability percentage was significantly or slightly above 70%, meaning that released ions did not show toxicity [81] at those concentrations. In Figure 5.7, cell viability test result is shown. Predominantly, ZA-2 and ZSA-2 exhibited rather high toxicity compared to ZA-1 and ZA-2. Still, for all of the samples, toxicity level was acceptable due to having higher than 70% viability. The control sample was tissue culture polystyrene in that case.

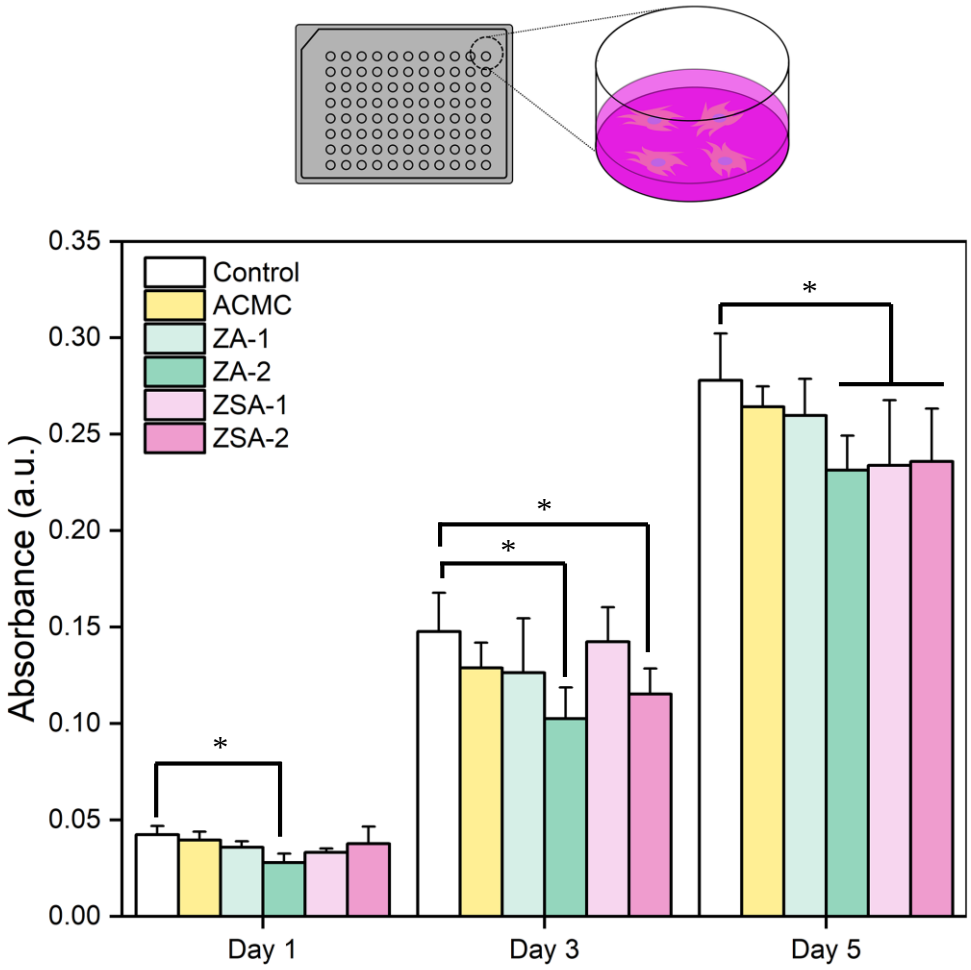

Figure 5.7 Fibroblast viability up to 5 days *in vitro*. Data are mean±SE, particle concentrations are 0.01 g/L

5.1.1.2 Antibacterial Performance

CFU assay was carried out to investigate the antibacterial activity against both Gram-positive (*S. aureus*) and Gram-negative (*E. coli*) bacteria. In Figure 5.8, antibacterial activity test results can be seen. Inherently non-toxic ACMC nanoparticles did not show antibacterial activity against both bacteria. Zinc incorporation clearly affected the performance of ACMC nanoparticles on *S. aureus.* ZA-1 and ZA-2 reduced the number

of bacteria by 13% and 36%. Dual incorporation of Zn and Sr intensified the effect. 29% and 56% declines were observed in ZSA-1 and ZSA-2. Whereas both single Zn dopant and dual Zn-Sr dopants reduced the bacterial growth of *S. aureus*, for *E. coli*, only dual dopant at higher concentration (ZSA-2) could be partially effective, decreasing bacteria by 16%.

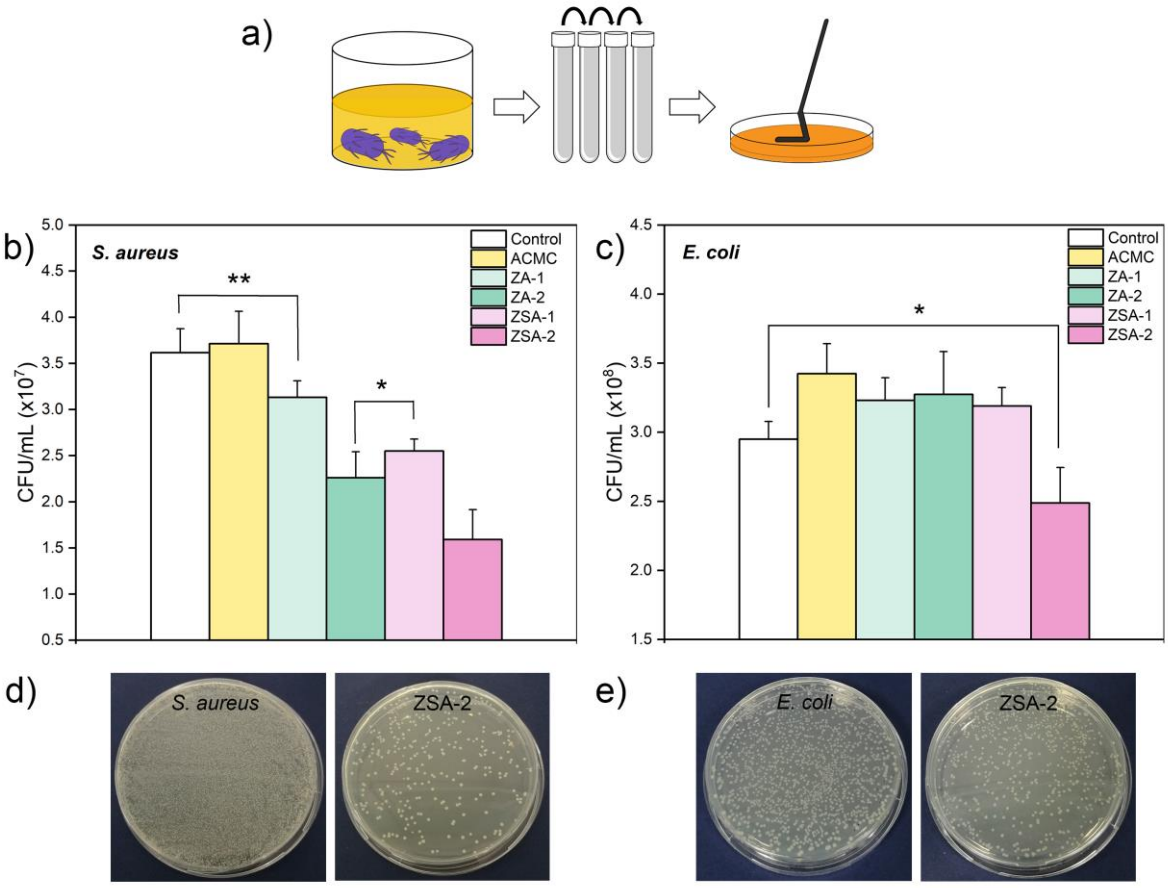

Figure 5.8 a) Schematics of the CFU assay. Antibacterial activity of the nanoparticles against b) *S. aureus* and c) *E. coli*, and agar photographs showing CFU of the control and ZSA-2 sample for d) *S. aureus* and e) *E. coli*. Data are mean ± SE, p*<0.05, particle concentrations are 0.01 g/L.

In summary, CFU assay results verified that ACMC nanoparticles gained antibacterial characteristic against *S. aureus* subsequent to Zn^{2+} ion incorporation. Antibacterial activity mechanism of Zn^{2+} ions is associated with reactive oxygen species (ROS) generation. ROS include several chemicals, such as superoxide anion radicals, hydroxyl radicals and hydrogen peroxides, and form through O_2 molecule and electron interactions. Those radicals are not able to pass through the membrane, yet harm the cellular components involving carbohydrate and lipid. On the contrary, hydrogen peroxide can easily diffuse into the cellular membrane and inhibit cellular proliferation [82]. ROS mechanism was not suggested based on bacterium type; however, there was an apparent contradiction between the antibacterial effect against *S. aureus* and *E.* coli. Likewise, in their study, where the antibacterial properties of bio-glass containing ZnO were investigated, Sergi et al. did not observe an antibacterial effect on Gram-negative bacteria: *E. coli* and *P. aeruginosa*, while growth of Gram-positive bacterium *S. epidermidis* could be considerably prohibited [81]. In spite of largely similar constituents, Gram-positive and Gram-negative bacteria differ in outer membrane structure. This difference makes Gram-negative bacteria more immune to antimicrobials. They have three layered thicker outer membrane, which is capable of blocking hydrophobic molecules and producing efflux pumps to dispose of antibiotics [83]. I believed that the contrasting result stemmed from the dissimilarity in outer membrane structure. The only sample which was relatively antibacterial against *E. coli* was ZSA-2. Additional Sr^{2+} ions intensified the antibacterial activity of Zn^{2+}, and that effect was dramatic on *S. aureus*. Yin et al. reported the synergistic effect of Zn^{2+} and Sr^{2+} ions on *S. mutants* and *P. gingivalis* [84]. Nevertheless, to be able to explain the reason why the ions together work more efficiently requires further studies.

CHAPTER 6

CONCLUSION AND FUTURE WORK

6.1 Conclusion

In this thesis, synthesis and antibacterial performance of ion incorporated magnesium stabilized amorphous calcium carbonate (ACMC) nanoparticles were investigated. The main contribution of this research into the scientific literature is the development of a synthesis protocol and introduction of novel ion incorporated ACMC nanoparticles.

In Chapter 4, SeO_3^{2-} ions were successfully incorporated into ACMC nanoparticles. ACMC nanoparticles maintained their particle size in the nanometer scale upon selenite incorporation. The results also revealed that the soluble nature of the nanoparticles led to decrease in colonies for both gram-positive (*S. aureus, S. epidermidis*) and gram-negative (*E. coli, P. aeruginosa*) bacteria strains. The antibacterial nature of the ACMC nanoparticles depended on the amount of selenite incorporation. Thus, Se-ACMC nanoparticles were proposed as an effective antibacterial material.

In Chapter 5, Zn^{2+} and Sr^{2+} ions were co-incorporated into ACMC nanoparticles while maintaining their nanometer size. Nanoparticles exhibited antibacterial activity against *S. aureus* at all ion concentrations, and the obtained antibacterial results increased with increased ion concentration (from 0.01 to 0.1 M). In fact, the combined effect of Zn^{2+} and Sr^{2+} partially reduced *E. coli* colony count at high concentrations. Furthermore, the cell viability assay demonstrated that synthesized nanoparticles were not cytotoxic at 0.01 g/L concentration

6.2 Future Work

This study fundamentally showed the possibility of incorporating SeO_3^{2-}, Zn^{2+} and Sr^{2+} ions into the ACMC structure. However, further improvements are required in the future to translate these nanoparticles for industrial and medical use. Despite obtaining ion incorporated stable ACMC nanoparticles, their solubility rate in Mg^{2+} free aqueous solutions was too rapid, which indicated a requirement for further stabilization of these nanoparticles. To improve the stability, the nanoparticles could be coated with several polymers, such as polyethylene glycol, polyacrylic acid or rhamnolipids. Polymer coatings can create steric hindrance and enhance the kinetic stability.

Since anticancer property of selenium and selenium oxyanions is an established fact, and ACC nanoparticles are frequently suggested as drug carriers, once a proper coating procedure is developed, Se-ACMC nanoparticles can be studied as carriers in drug delivery systems to target cancerous cells.

Moreover, to understand the synergistic effect of Zn^{2+} and Sr^{2+} ions against bacteria, further characterizations, such as bacteria live/dead assay, SEM images of bacteria and ROS generation studies can be performed. Likewise, for cytotoxicity assay SEM images of L929 cells should be taken to understand the morphology of the cells.

REFERENCES

[1] P. D. Morris, I. J. Mcpherson, G. N. Meloni, and P. R. Unwin, "Nanoscale kinetics of amorphous calcium carbonate precipitation in H_2O and D_2O," *Physical Chemistry Chemical Physics*, vol. 22, p. 22107, 2020, doi: 10.1039/d0cp03032e.

[2] J. S. Han, S. Y. Jung, D. S. Kang, and Y. B. Seo, "Development of Flexible Calcium Carbonate for Papermaking Filler," *ACS Sustainable Chemistry and Engineering*, vol. 8, no. 24, pp. 8994–9001, 2020, doi: 10.1021/acssuschemeng.0c01593/asset/images/large/sc0c01593_0008.jpeg.

[3] E. Mugnaioli, I. Andrusenko, T. Schüler, N. Loges, R. E. Dinnebier, M. Panthöfer, W. Tremel, and U. Kolb, "Vaterite Structure Ab Initio Structure Determination of Vaterite by Automated Electron Diffraction", *Angewandte Chemie International Edition*, vol. 51, pp. 7041-7045, 2012, doi: 10.1002/anie.201200845.

[4] H. Marschner, "Hydrocalcite ($CaCO_3 \cdot H_2O$) and Nesquehonite ($MgCO_3 \cdot 3H_2O$) in Carbonate Scales," *Science (1979)*, vol. 165, no. 3898, pp. 1119–1121, 1969, doi: 10.1126/science.165.3898.1119.

[5] G. Marland, "The stability of CaCO3·6H2O (ikaite)," *Geochimica et Cosmochimica Acta*, vol. 39, no. 1, pp. 83–91, 1975, doi: 10.1016/0016-7037(75)90186-6.

[6] B. Myszka, M. Schüßler, K. Hurle, B. Demmert, R. Detsch, A. R. Boccaccini, and S. E. Wolf, "Phase-specific bioactivity and altered Ostwald ripening pathways of calcium carbonate polymorphs in simulated body fluid," *RSC Advances*, 2019, doi: 10.1039/c9ra01473j.

[7] L. B. Gower, "Biomimetic model systems for investigating the amorphous precursor pathway and its role in biomineralization," *Chemical Reviews*, vol.

108, no. 11, pp. 4551–4627, 2008, doi: 10.1021/cr800443h/asset/images/large/cr-2008-00443h_0045.jpeg.

[8] M. Farhadi-Khouzani, D. M. Chevrier, P. Zhang, N. Hedin, and D. Gebauer, "Water as the Key to Proto-Aragonite Amorphous CaCO3," *Angewandte Chemie - International Edition*, vol. 55, no. 28, pp. 8117–8120, 2016, doi: 10.1002/anie.201603176.

[9] A. V. Radha, T. Z. Forbes, C. E. Killian, P. U. P. A. Gilbert, and A. Navrotsky, "Transformation and crystallization energetics of synthetic and biogenic amorphous calcium carbonate," *Proceedings of National Academy of Sciences USA*, vol. 107, no. 38, pp. 16438–16443, 2010, doi: 10.1073/pnas.1009959107/suppl_file/pnas.1009959107_si.pdf.

[10] M. Albéric, L. Bertinetti, Z. Zou, P. Fratzl, W. Habraken, and Y. Politi, "The Crystallization of Amorphous Calcium Carbonate is Kinetically Governed by Ion Impurities and Water," *Advanced Science*, vol. 5, no. 5, p. 1701000, 2018, doi: 10.1002/advs.201701000.

[11] C. L. Freeman, J. H. Harding, D. Quigley, and P. M. Rodger, "How does an amorphous surface influence molecular binding? – ovocleidin-17 and amorphous calcium carbonate," *Physical Chemistry Chemical Physics*, vol. 17, no. 26, pp. 17494–17500, 2015, doi: 10.1039/C5CP00434A.

[12] M. S. Saveleva, K. Eftekhari, A. Abalymov, T. E. L. Douglas, D. Volodkin, B. V. Parakhonskiy, and A. G. Skirtach, "Hierarchy of hybrid materials-the place of inorganics-*in*-organics in it, their composition and applications," *Frontiers in Chemistry*, vol. 7, p. 179, 2019, doi: 10.3389/fchem.2019.00179/bibtex.

[13] L. Fernández-Díaz, J. M. Astilleros, and C. M. Pina, "The morphology of calcite crystals grown in a porous medium doped with divalent cations," *Chemical Geology*, vol. 225, no. 3–4, pp. 314–321, 2006, doi: 10.1016/j.chemgeo.2005.08.024.

[14] S. H. Yu, H. Li, Q. Z. Yao, G. T. Zhou, and S. Q. Fu, “Preparation of mesoporous calcite with hierarchical architectures,” *Materials Letters*, vol. 160, pp. 167–170, 2015, doi: 10.1016/J.MATLET.2015.07.116.

[15] A. Samanta, S. Podder, M. Kumarasamy, C. K. Ghosh, D. Lahiri, P. Roy, S. Bhattacharjee, J. Ghosh, and, A. K. Mukhopadhyay, “Au nanoparticle-decorated aragonite microdumbbells for enhanced antibacterial and anticancer activities,” *Materials Science and Engineering C*, vol. 103, 2019, doi: 10.1016/j.msec.2019.05.019.

[16] R. Febrida, A. Cahyanto, E. Herda, V. Muthukanan, N. Djustiana, F. Faizal, C. Panatarani, and M. Joni, “Materials Synthesis and Characterization of Porous $CaCO_3$ Vaterite Particles by Simple Solution Method,” *Materials*, vol. 14, 2021, doi: 10.3390/ma14164425.

[17] J. Dou, F. Zhao, W. Fan, Z. Chen, and X. Guo, “Preparation of non-spherical vaterite $CaCO_3$ particles by flash nano precipitation technique for targeted and extended drug delivery,” *Journal of Drug Delivery Science and Technology*, vol. 57, 2020, doi: 10.1016/j.jddst.2020.101768.

[18] C. Wang, S. Chen, Q. Yu, F. Hu, and H. Yuan, “Taking advantage of the disadvantage: employing the high aqueous instability of amorphous calcium carbonate to realize burst drug release within cancer cells,” *Journal of Materials Chemistry B*, vol. 5, no. 11, pp. 2068–2073, 2017, doi: 10.1039/c6tb02826h.

[19] J. T. Avaro, C. Ruiz-Agudo, E. Landwehr, K. Hauser, and D. Gebauer, “Impurity-free amorphous calcium carbonate, a preferential material for pharmaceutical and medical applications,” *European Journal of Mineralogy*, vol. 31, no. 2, pp. 231–236, 2019, doi: 10.1127/ejm/2019/0031-2831.

[20] Z. Zou, X. Yang, M. Albéric, T. Heil, Q. Wang, B. Pokroy, Y. Politi, and L. Bertinetti., “Additives Control the Stability of Amorphous Calcium Carbonate via Two Different Mechanisms: Surface Adsorption versus Bulk

Incorporation," *Advanced Functional Materials*, vol. 30, no. 23, p. 2000003, 2020, doi: 10.1002/ADFM.202000003.

[21] L. Addadi, S. Raz, and S. Weiner, "Taking Advantage of Disorder: Amorphous Calcium Carbonate and Its Roles in Biomineralization," *Advanced Materials*, vol. 15, no. 12, pp. 959–970, 2003, doi: 10.1002/adma.200300381.

[22] T. Jeon, Y. E. Na, D. Jang, and I. W. Kim, "Stabilized Amorphous Calcium Carbonate as a Precursor of Microcoating on Calcite," *Materials 2020, Vol. 13*, vol. 13, no. 17, p. 3762, 2020, doi: 10.3390/ma13173762.

[23] R. Sandya Rani and M. Saharay, "Molecular dynamics simulation of protein-mediated biomineralization of amorphous calcium carbonate," *RSC Advances*, 2019, doi: 10.1039/c8ra08459a.

[24] Y. W. Wang, Y. Y. Kim, C. J. Stephens, F. C. Meldrum, and H. K. Christenson, "In Situ Study of the Precipitation and Crystallization of Amorphous Calcium Carbonate (ACC)," *Crystal Growth and Design*, vol. 12, pp. 1212-1217, 2012, doi: 10.1021/cg201204s.

[25] C. Rao, M. Li, X. Sun, M. Li, X. Lian, H. Wang, L. Jia, B. Niu, and W. Li, "Preparation and characterization of phosphate-stabilized amorphous calcium carbonate nanoparticles and their application in curcumin delivery," *Materials Chemistry and Physics*, vol. 255, p. 123552, 2020, doi: 10.1016/J.Matchemphys.2020.123552.

[26] U. P. A. Gilbert, K. D. Bergmann, N. Boekelheide, S. Tambutte, and A. H. Knoll, "Biomineralization: Integrating mechanism and evolutionary history," *Science Advances*, vol. 8, no. 10, 2022, doi: 10.1126/sciadv.abl9653.

[27] J. Ihli, W. C. Wong, E. H. Noel, Y. Y. Kim, A. N. Kulak, H. K. Christenson, M. J. Duer, F. C. Meldrum, "Dehydration and crystallization of amorphous

calcium carbonate in solution and in air," *Nature Communications*, vol. 5, 2014, doi: 10.1038/ncomms4169.

[28] Y. C. Huang, M. B. Gindele, J. Knaus, A. Rao, and D. Gebauer, "On mechanisms of mesocrystal formation: magnesium ions and water environments regulate the crystallization of amorphous minerals," *CrystEngComm*, vol. 20, pp. 4395-4405, 2018, doi:https://doi.org/10.1039/c8ce00241j

[29] C. C. Xue, M. H. Li, Y. Zhao, J. Zhou, Y. Hu, K. Y. Cai, Y. Zhao, S. H. Yu, and Z. Luo "Tumor microenvironment-activatable Fe-doxorubicin preloaded amorphous $CaCO_3$ nanoformulation triggers ferroptosis in target tumor cells," *Science Advances*, vol. 6, no. 18, 2020, doi: 10.1126/sciadv.aax1346/suppl_file/aax1346_sm.pdf.

[30] L. Dong, Y. J. Xu, C. Sui, Y. Zhao, L. B. Mao, D. Gebauer, R. Rosenberg, J. Avaro, Y. D. Wu, H. L. Gao, Z. Pan, H. Q. Wen, X. Yan, F. Li, Y. Lu, H. Cölfen, and S. H. Yu., "Highly hydrated paramagnetic amorphous calcium carbonate nanoclusters as an MRI contrast agent," *Nature Communications*, vol. 13, no. 1, pp. 1–13, 2022, doi: 10.1038/s41467-022-32615-3.

[31] N. Xu., "Synthesis and application of magnesium amorphous calcium carbonate for removal of high concentration of phosphate," *Chemical Engineering Journal*, vol. 251, pp. 102–110, 2014, doi: 10.1016/j.cej.2014.04.037.

[32] X. Jia, B. Kayitmazer, A. Ahmad, N. Ramzan, Y. Li, Y. Xu, and S. Sun., "Polyacids for producing colloidally stable amorphous calcium carbonate clusters in water," *Journal of Applied Polymer Science*, vol. 139, no. 14, p. 51899, 2022, doi: 10.1002/app.51899.

[33] E. Tolba *et al.*, "molecules Self-Healing Properties of Bioinspired Amorphous $CaCO_3$ /Polyphosphate-Supplemented Cement", *Molecules*, vol. 25, no. 10, p. 2360, 2020, doi: 10.3390/molecules25102360.

[34] H. Shaked, I. Polishchuk, A. Nagel, Y. Bekenstein, and B. Pokroy, “Long-term stabilized amorphous calcium carbonate—an ink for bio-inspired 3D printing,” *Materials Today Bio*, vol. 11, p. 100120, 2021, doi: 10.1016/j.mtbio.2021.100120.

[35] G. Y. Jung, E. Shin, J. H. Park, B. Y. Choi, S. W. Lee, and S. K. Kwak, “Thermodynamic Control of Amorphous Precursor Phases for Calcium Carbonate via Additive Ions,” *Chemistry of Materials*, vol. 31, no. 18, pp. 7547–7557, 2019, doi: 10.1021/acs.chemmater.9b02346/asset/images/medium/cm9b02346_m009.gif.

[36] X. Lv *et al.*, “Recent Nanotechnologies to Overcome the Bacterial Biofilm Matrix Barriers,” *Small*, p. 2206220, 2022, doi: 10.1002/smll.202206220.

[37] H. Dong *et al.*, “Biofilm microenvironment response nanoplatform synergistically degrades biofilm structure and relieves hypoxia for efficient sonodynamic therapy,” *Chemical Engineering Journal*, vol. 453, 2023, doi: 10.1016/j.cej.2022.139839.

[38] T. Pulingam *et al.*, “Antimicrobial resistance: Prevalence, economic burden, mechanisms of resistance and strategies to overcome,” *European Journal of Pharmaceutical Sciences*, vol. 170, 2022, doi: 10.1016/j.ejps.2021.106103.

[39] X. Kong, X. Liu, Y. Zheng, P. K. Chu, Y. Zhang, and S. Wu, “Graphitic carbon nitride-based materials for photocatalytic antibacterial application,” *Materials Science and Engineering R: Reports*, vol. 145, 2021, doi: 10.1016/j.mser.2021.100610.

[40] X. Li, H. Bai, Y. Yang, J. Yoon, S. Wang, and X. Zhang, “Supramolecular Antibacterial Materials for Combatting Antibiotic Resistance,” *Advanced Materials*, vol. 31, no. 5, p. 1805092, 2019, doi: 10.1002/adma.201805092.

[41] N. Niño-Martínez, M. Felipe, S. Orozco, G.-A. Martínez-Castañón, F. Torres Méndez, and F. Ruiz, “Molecular Sciences Molecular Mechanisms of

Bacterial Resistance to Metal and Metal Oxide Nanoparticles", *International Journal of Molecular Sciences*, 2019, doi: 10.3390/ijms20112808.

[42] F. Chen *et al.*, "2D Molybdenum Sulfide-Based Materials for Photo-Excited Antibacterial Application," *Advanced Healthcare Materials*, vol. 11, no. 13, p. 2200360, 2022, doi: 10.1002/adhm.202200360.

[43] H.-W. Han *et al.*, "Selenium Nanoparticles as Candidates for Antibacterial Substitutes and Supplements against Multidrug-Resistant Bacteria," Biomolecules, vol. 11, p. 1028, doi: 10.3390/biom11071028.

[44] J. Ge *et al.*, "Comparison of nanoparticle-selenium, selenium-enriched yeast and sodium selenite on the alleviation of cadmium-induced inflammation via NF-kB/IκB pathway in heart," *Science of The Total Environment*, vol. 773, p. 145442, 2021, doi: 10.1016/j.scitotenv.2021.145442.

[45] H. Deng *et al.*, "Progress of Selenium Deficiency in the Pathogenesis of Arthropathies and Selenium Supplement for Their Treatment," *Biological Trace Element Research*, vol. 200, no. 10, pp. 4238–4249, 2021, doi: 10.1007/S12011-021-03022-4.

[46] V. W. Kilonzo *et al.*, "Juvenile Selenium Deficiency Impairs Cognition, Sensorimotor Gating, and Energy Homeostasis in Mice," *Frontiers in Nutrition*, vol. 8, p. 209, 2021, doi: 10.3389/fnut.2021.667587/bibtex.

[47] Y. Huang, E. Su, J. Ren, and X. Qu, "The recent biological applications of selenium-based nanomaterials," *Nano Today*, vol. 38, 2021, doi: 10.1016/j.nantod.2021.101205.

[48] V. Uskoković, M. A. Iyer, and V. M. Wu, "One ion to rule them all: the combined antibacterial, osteoinductive and anticancer properties of selenite-incorporated hydroxyapatite," *Journal of Materials Chemistry B*, vol. 5, no. 7, pp. 1430–1445, 2017, doi: 10.1039/c6tb03387c.

[49] M. F. Alam, M. M. Safhi, S. S. Moni, and A. Jabeen, “In Vitro Antibacterial Spectrum of Sodium Selenite against Selected Human Pathogenic Bacterial Strains,” *Scientifica (Cairo)*, vol. 2016, 2016, doi: 10.1155/2016/9176273.

[50] X. Zhang, W. Y. Fan, M. C. Yao, C. W. Yang, and G. P. Sheng, “Redox state of microbial extracellular polymeric substances regulates reduction of selenite to elemental selenium accompanying with enhancing microbial detoxification in aquatic environments,” *Water Research*, vol. 172, 2020, doi: 10.1016/j.watres.2020.115538.

[51] S. Lampis *et al.*, “Selenite biotransformation and detoxification by Stenotrophomonas maltophilia SeITE02: Novel clues on the route to bacterial biogenesis of selenium nanoparticles,” *Journal of Hazardous Materials*, vol. 324, pp. 3–14, 2017, doi: 10.1016/j.jhazmat.2016.02.035.

[52] T. Huang, J. A. Holden, E. C. Reynolds, D. E. Heath, N. M. O’Brien-Simpson, and A. J. O’Connor, “Multifunctional Antimicrobial Polypeptide-Selenium Nanoparticles Combat Drug-Resistant Bacteria,” *ACS Applied Materials and Interfaces*, vol. 12, no. 50, pp. 55696–55709, 2020, doi: 10.1021/acsami.0c17550/asset/images/medium/am0c17550_m001.gif.

[53] J. A. Lemire, J. J. Harrison, and R. J. Turner, “Antimicrobial activity of metals: Mechanisms, molecular targets and applications,” *Nature Reviews Microbiology*, vol. 11, no. 6. pp. 371–384, 2013. doi: 10.1038/nrmicro3028.

[54] V. Luque-Agudo, M. C. Fernández-Calderón, M. A. Pacha-Olivenza, C. Pérez-Giraldo, A. M. Gallardo-Moreno, and M. L. González-Martín, “The role of magnesium in biomaterials related infections,” *Colloids and Surfaces B: Biointerfaces*, vol. 191, 2020, doi: 10.1016/j.colsurfb.2020.110996.

[55] R. Villa-Bellosta, “Dietary magnesium supplementation improves lifespan in a mouse model of progeria,” *EMBO Molecular Medicine*, vol. 12, no. 10, p. 2423, 2020, doi: 10.15252/emmm.202012423.

[56] H. Feng *et al.*, “Systematic Study of Inherent Antibacterial Properties of Magnesium-based Biomaterials,” *ACS Applied Materials and Interfaces*, vol. 8, p. 42, 2016, doi: 10.1021/acsami.6b02241.

[57] H. Peng *et al.*, “Degradable magnesium implants inhibit gallbladder cancer,” *Acta Biomaterialia*, vol. 128, pp. 514–522, Jul. 2021, doi: 10.1016/j.actbio.2021.04.051.

[58] L. Wang *et al.*, “Antibacterial Composite Materials Based on the Combination of Polyhydroxyalkanoates With Selenium and Strontium Co-substituted Hydroxyapatite for Bone Regeneration,” *Frontiers in Bioengineering and* Biotechnology, vol. 9, 2021, doi: 10.3389/fbioe.2021.647007.

[59] C. Y. Wang, Y. C. Chiu, A. Kai, X. Lee, Y. A. Lin, P. Y. Lin, and M. Y. Shie, “Biofabrication of Gingival Fibroblast Cell-Laden Collagen/Strontium-Doped Calcium Silicate 3D-Printed Bi-Layered Scaffold for Osteoporotic Periodontal Regeneration,” Biomedicines, 2021, doi: 10.3390/biomedicines9040431.

[60] K. Qiu, X. J. Zhao, C. X. Wan, C. S. Zhao, and Y. W. Chen, “Effect of strontium ions on the growth of ROS17/2.8 cells on porous calcium polyphosphate scaffolds,” *Biomaterials*, vol. 27, no. 8, pp. 1277–1286, Mar. 2006, doi: 10.1016/j.biomaterials.2005.08.006.

[61] S. Shao *et al.*, “A titanium surface modified with zinc-containing nanowires: Enhancing biocompatibility and antibacterial property in vitro,” *Applied Surface Science*, vol. 515, Jun. 2020, doi: 10.1016/j.apsusc.2020.146107.

[62] Chetan and U. Vijayalakshmi, “Evaluating the induction of antibacterial properties upon zinc incorporation in strontium phosphosilicate for bone regeneration applications,” *Materials Letters*, vol. 309, p. 131303, 2022, doi: 10.1016/j.matlet.2021.131303.

[63] A. A. Tayel *et al.*, “Antibacterial action of zinc oxide nanoparticles against foodborne pathogens,” *Journal of Food Safety*, vol. 31, no. 2, pp. 211–218, May 2011, doi: 10.1111/j.1745-4565.2010.00287.x.

[64] A. A. Tayel *et al.*, “Antibacterial Action Of Zinc Oxide Nanoparticles Against Foodborne Pathogens,” *Journal of Food Safety*, vol. 31, no. 2, pp. 211–218, May 2011, doi: 10.1111/j.1745-4565.2010.00287.x.

[65] S. Cheeseman *et al.*, “Antimicrobial Metal Nanomaterials: From Passive to Stimuli-Activated Applications,” *Advanced Science*, vol. 7, no. 10, 2020, doi: 10.1002/advs.201902913.

[66] M. Godoy-Gallardo *et al.*, “Antibacterial approaches in tissue engineering using metal ions and nanoparticles: From mechanisms to applications,” *Bioactive Materials*, vol. 6, no. 12, pp. 4470–4490, 2021, doi: 10.1016/j.bioactmat.2021.04.033.

[67] C. Xu *et al.*, “Biodegradable Nanoparticles of Polyacrylic Acid–Stabilized Amorphous CaCO3 for Tunable pH-Responsive Drug Delivery and Enhanced Tumor Inhibition,” *Advanced Functional Materials*, vol. 29, no. 24, p. 1808146, 2019, doi: 10.1002/adfm.201808146.

[68] S. Dhatchayani, S. Vijayakumar, N. Sarala, B. Vaseeharan, and K. Sankaranarayanan, “Effect of curcumin sorbed selenite substituted hydroxyapatite on osteosarcoma cells: An in vitro study,” *Journal of Drug Delivery Science and Technology*, vol. 60, 2020, doi: 10.1016/j.jddst.2020.101963.

[69] S. Zhang *et al.*, “Magnesium Ions Direct the Solid-State Transformation of Amorphous Calcium Carbonate Thin Films to Aragonite, Magnesium-Calcite, or Dolomite,” *Advanced Functional Materials*, vol. 32, 2022, doi: 10.1002/adfm.202201394.

[70] C. Ferro, H. F. Florindo, and H. A. Santos, “Selenium Nanoparticles for Biomedical Applications: From Development and Characterization to

Therapeutics," *Advanced Healthcare Materials*, vol. 10, no. 16, Aug. 2021, doi: 10.1002/adhm.202100598.

[71] H. Fernández-Llamosas, L. Castro, M. Luisa Blázquez, E. Díaz, and M. Carmona, "Speeding Up Bioproduction Of Selenium Nanoparticles By Using Vibrio Natriegens As Microbial Factory OPEN", *Scientific Reports*, doi: 10.1038/s41598-017-16252-1.

[72] J. Wang *et al.*, "Calcium Supplement by Tetracycline guided amorphous Calcium Carbonate potentiates Osteoblast promotion for Synergetic Osteoporosis Therapy," *Theranostics*, vol. 10, no. 19, pp. 8591–8605, 2020, doi: 10.7150/THNO.45142.

[73] W. E. G. Müller *et al.*, "Amplified Morphogenetic And Bone Forming Activity Of Amorphous Versus Crystalline Calcium Phosphate/Polyphosphate," *Acta Biomaterialia*, vol. 118, pp. 233–247, 2020, doi: 10.1016/J.ACTBIO.2020.10.023.

[74] M. Jiménez, C. Abradelo, J. San Román, and L. Rojo, "Bibliographic Review On The State Of The Art Of Strontium And Zinc Based Regenerative Therapies. Recent Developments And Clinical Applications," *Journal of Materials Chemistry B*, vol. 7, no. 12, pp. 1974–1985, 2019, doi: 10.1039/c8tb02738b.

[75] Z. Zhong *et al.*, "Zn/Sr dual ions-collagen co-assembly hydroxyapatite enhances bone regeneration through procedural osteo-immunomodulation and osteogenesis," *Bioactive Materials*, vol. 10, pp. 195–206, 2022, doi: 10.1016/j.bioactmat.2021.09.013.

[76] Y. Li, D. Zhang, Z. Wan, X. Yang, and Q. Cai, "Dental resin composites with improved antibacterial and mineralization properties via incorporating zinc/strontium-doped hydroxyapatite as functional fillers," *Biomedical Materials*, vol. 17, no. 4, p. 045002, 2022, doi: 10.1088/1748-605X/AC6B72.

[77] V. Sharma, S. Basak, K. Rishabh, H. Umaria, and S. W. Ali, “Synthesis of zinc carbonate nanoneedles, a potential flame retardant for cotton textiles,” *Cellulose*, vol. 25, no. 10, pp. 6191–6205, 2018, doi: 10.1007/S10570-018-1962-5/figures/10.

[78] P. Lu *et al.*, “One-step preparation of a novel $SrCO_3$ /g-C_3N_4 nano-composite and its application in selective adsorption of crystal violet,” *RSC Advances*, 2018, doi: 10.1039/c7ra11565b.

[79] S. T. Mergelsberg, J. J. de Yoreo, Q. R. S. Miller, F. Marc Michel, R. N. Ulrich, and P. M. Dove, “Metastable solubility and local structure of amorphous calcium carbonate (ACC),” *Geochimica Cosmochimica Acta*, vol. 289, pp. 196–206, 2020, doi: 10.1016/j.gca.2020.06.030.

[80] Y. Huang *et al.*, “Facile Synthesis of Zn^{2+}-Based Hybrid Nanoparticles as a New Paradigm for the Treatment of Internal Bacterial Infections,” *Advanced Functional Materials*, vol. 32, no. 15, p. 2109011, 2022, doi: 10.1002/adfm.202109011.

[81] R. Sergi, D. Bellucci, R. Salvatori, G. Maisetta, G. Batoni, and V. Cannillo, “Zinc containing bioactive glasses with ultra-high crystallization temperature, good biological performance and antibacterial effects,” *Materials Science and Engineering: C*, vol. 104, p. 109910, 2019, doi: 10.1016/j.msec.2019.109910.

[82] D. E. Navarro-López *et al.*, “Effective antimicrobial activity of ZnO and Yb-doped ZnO nanoparticles against Staphylococcus aureus and Escherichia coli,” *Materials Science and Engineering: C*, vol. 123, p. 112004, 2021, doi: 10.1016/j.msec.2021.112004.

[83] P. Makvandi *et al.*, “Metal-Based Nanomaterials in Biomedical Applications: Antimicrobial Activity and Cytotoxicity Aspects,” *Advanced Functional Materials*, vol. 30, no. 22, p. 1910021, 2020, doi: 10.1002/adfm.201910021.

[84] S. Yin *et al.*, “The Translation from in Vitro Bioactive Ion Concentration Screening to in Vivo Application for Preventing Peri-implantitis,” *ACS Applied Materials and Interfaces*, vol. 13, no. 4, pp. 5782–5794, 2021, doi: 10.1021/acsami.0c19698/asset/images/large/am0c19698_0011.jpeg.